Texas A&M University
Mechanical Engineering Department
Turbomachinery Laboratory
Tribology Group

GAS LABYRINTH SEALS: ON THE EFFECT OF CLEARANCE AND OPERATING CONDITIONS ON WALL FRICTION FACTORS – A CFD INVESTIGATION

TRC-SEAL-02-18

Research Progress Report to the Turbomachinery Research Consortium
by

Luis San Andrés
Mast-Childs Chair Professor
Principal Investigator

Tingcheng Wu
Research Assistant

May 2018

PRESSING NEEDS FOR SEALS /BEARING SOFTWARE DEVELOPMENT/UPDATE
TRC Project, TEES # 400124-00099

EXECUTIVE SUMMARY

Bulk-flow predictive models, though simple and fast, often fail to accurately predict the performance of gas labyrinth seals (LSs). Presently, a CFD analysis quantifies the effects of labyrint LS tip clearance (C_r) and operating conditions on the friction factors (f_r, f_s) at the rotor and stator surfaces, along the circumferential direction. The analysis aims to improve the prediction of LS dynamic force coefficients, in particular the evolution of the circumferential flow velocity and the seal cross-coupled stiffness. A fourteen teeth on stator LS seal (L/D=0.29) with clearance C_r=1/733 D is selected for analysis. The seal operates at nominal supply and discharge pressures equal to 73 bar and 51 bar, respectively, and at a rotor speed of 12 krpm (surface speed=138 m/s.).

The analysis models the seal with a fine mesh of a few million nodes and a commercial CFD code calculates the flow field for the nominal operating conditions, as well as for changes in clearance, 20% above and below C_r, shaft speed from 5 krpm to 15 krpm (58 m/s ~173 m/s), inlet pre-swirl velocity varying from 42% to 72% of rotor surface speed, a gas supply pressure ranging from 60 bar to 100 bar, and along with various discharge pressures producing a pressure ratio (PR) ranging from 0.40 to 0.85. The numerous predictions output the wall shear stresses as well as the bulk-flow velocity and frictions factors. The rotor surface friction factor f_r is independent of the (modest) changes in clearance (C_r) or the inlet presiwrl ratio; whereas an increase in rotor speed or pressure ratio (PR) decreases f_r. On the other hand, an increase in rotor speed, pressure ratio and inlet preswirl ratio decreases f_s, the stator friction factor. Besides, f_s increases with an increase in radial clearance. Further, f_r and f_s are only sensitive to the pressure ratio, but not to the magnitude of the supply pressure or discharge pressure.

Lastly, The CFD predictions produce new coeffients for the classical Blasius friction factor model, $f=n\ R_e^m$, with R_e as a bulk-flow Reynolds number relative to a wall. Later, integration of the found f's into a BFM code will improve its accuracy to predict the evolution of the circumerential flow velocity and the seal rotordynamic force coefficients.

TABLE OF CONTENTS

LIST OF FIGURES

LIST OF TABLES

1. INTRODUCTION

Commonly found in gas and steam turbines and compressors, labyrinth seals (LS) control the leakage (secondary flow) from a high pressure region to a low pressure region. A typical LS comprises of cavities and teeth facing a spinning rotor. The tortuous gas flow path through the cavities induces a pressure drop and restricts leakage. A see-through LS has all the teeth either on the rotor (TOR) or on the stator (TOS), while an interlocking design (ILS) has teeth on the rotor as well as on the stator. LS leakage depends on seal geometry (tooth shape, pitch/depth, and number of cavities), gas type, and operating shaft speed, pressure and temperature (inlet and outlet).

During operation, seals do not just restrict a secondary flow but also produce reaction forces acting on the rotor. These forces may introduce an instability into a rotating system, as reported in Refs. [1, 2] for example. Therefore, the ability to accurately predict LS leakage and rotordynamic force coefficients is crucial for the efficient and rotordynamic stable operation of turbomachinery.

Forces developed by LSs are typically lower than those in liquid seals. For small amplitude rotor displacements (X,Y) about its centered condition, the force components (F_X, F_Y) are modeled as

$$-\begin{bmatrix} F_X \\ F_Y \end{bmatrix} = \begin{bmatrix} K_{(\omega)} & k_{(\omega)} \\ -k_{(\omega)} & K_{(\omega)} \end{bmatrix} \begin{bmatrix} X \\ Y \end{bmatrix} + \begin{bmatrix} C_{(\omega)} & c_{(\omega)} \\ -c_{(\omega)} & C_{(\omega)} \end{bmatrix} \begin{bmatrix} \dot{X} \\ \dot{Y} \end{bmatrix} \tag{1}$$

where ($K_{(\omega)}$, $C_{(\omega)}$) stand for the direct stiffness and damping coefficients; and ($k_{(\omega)}$, $c_{(\omega)}$) for the cross-coupled stiffness and damping, respectively. In a gas seal the force coefficients are functions of the excitation frequency (ω). LSs, because of the working gas small density[1], offer negligible added mass terms.

The literature is profuse on detailing experimental results and models for LS leakage and rotordynamic coefficients [2]. Most research focuses on "see-through" LSs, that is seals with a uniform clearance and all the teeth on either the stator (TOS), see Figure 1 (a), or all on the rotor (TOR), see Figure 1(b).

[1] This assertion is not valid for seals handing sCO_2 (at high pressures), for example.

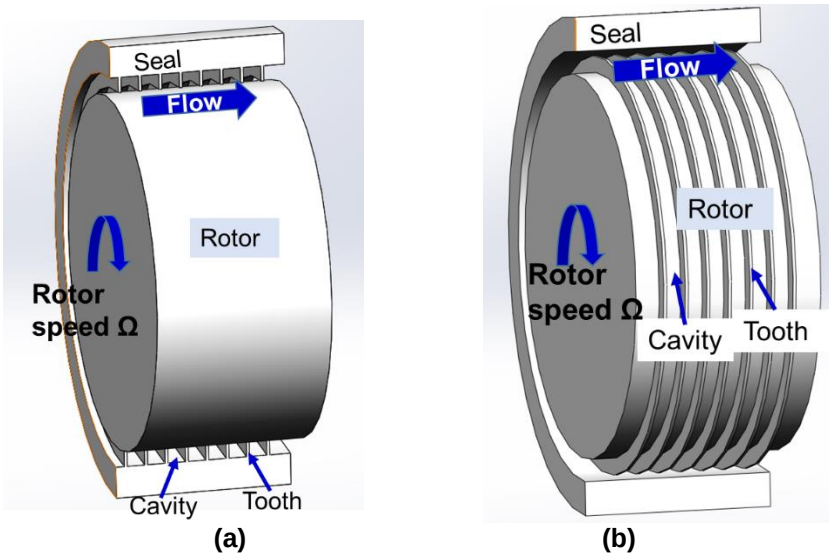

Figure 1. See through labyrinth gas seal: (a) teeth on stator (TOS), (b) teeth on rotor (TOR).

The interlocking labyrinth seal (ILS) configuration, as shown in Figure 2, increases the overall flow resistance as the gas passes through a narrow clearance. Therefore, the ILS relatively leaks less compared to conventional TOS and TOR LS designs. As shown in Figure 3, the flow moves through a tortuous path and displays two regimes; namely a core flow and recirculation zones in the cavities. The core flow is a jet through flow in the leakage path which plays a dominant role in determining seal leakage. The recirculation zones in a cavity contribute to mechanical energy dissipation.

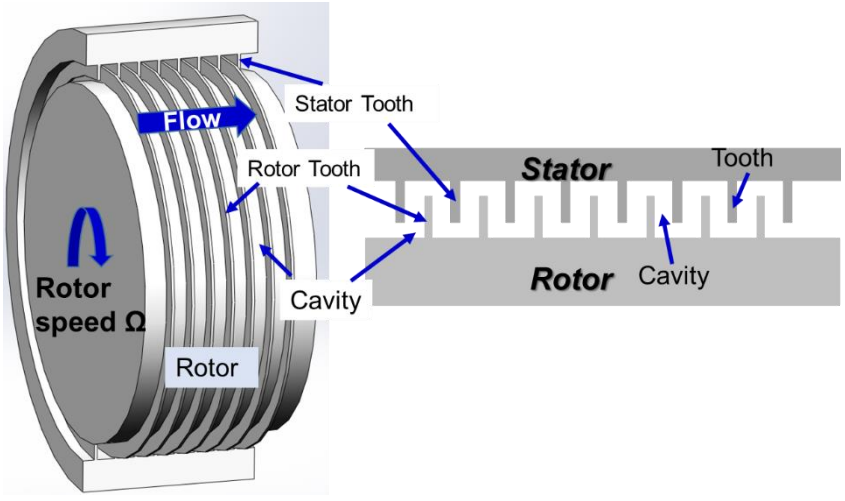

Figure 2. Interlocking labyrinth gas seal.

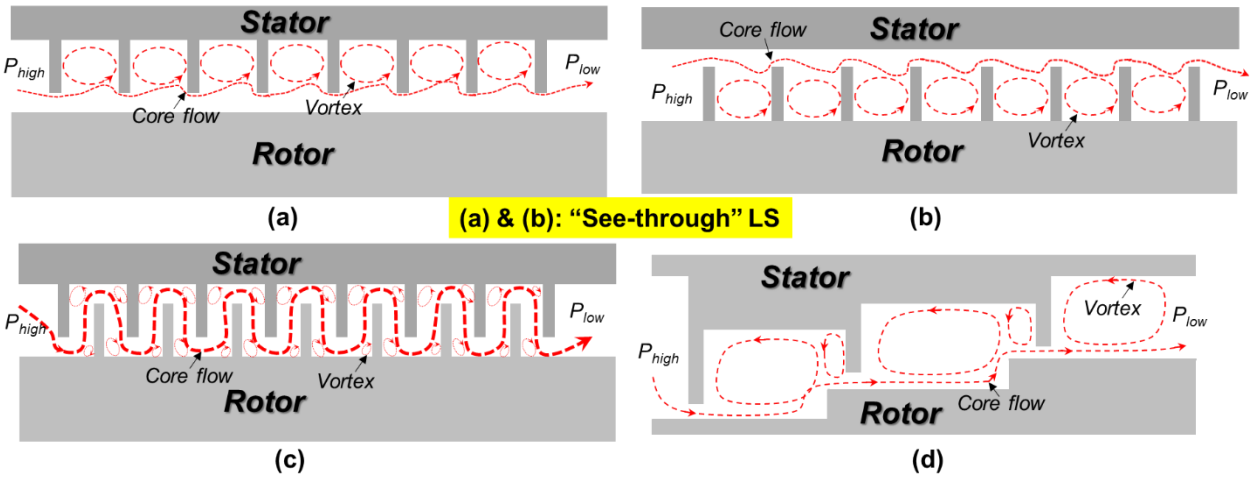

Figure 3. Schematic views of flow passing through the clearance channel in a seal: (a) TOS, (b) TOR, (c) ILS, (d) stepped LS [3].

Recently, using a CFD approach, Kuwamura et al. [3] developed a new high-performance labyrinth seal, see Figure 4. This improved LS design reduces leakage up to 30% when compared to conventional *see-through* labyrinth seals.

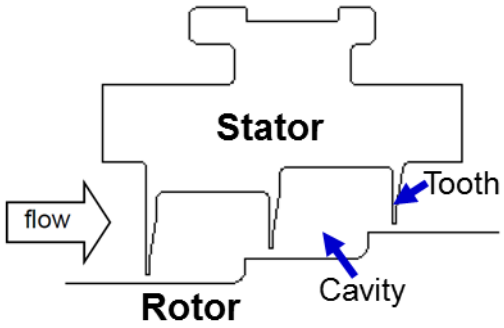

Figure 4. Improved (stepped)labyrinth gas seal [3].

A modern compressor balance drum usually employs an interlocking labyrinth seal (ILS) to hold a higher pressure drop, and thus this seal has a significant influence on rotor stability [4]. However, scant results for either interlocking LS or the stepped labyrinth seals are available.

The primary objective of the present work is to advance an accurate prediction model for LSs with correlations derived through a CFD investigation of the flow field in typical labyrinth gas seals. The CFD analysis produces a relation between wall friction factor and operating conditions. Integration of the CFD derived wall friction factor relations into the BFM contributes to an improved accuracy.

2. REVIEW OF PAST LITERATURE[2]

This review first assesses experimental works on labyrinth seals and next discusses the various numerical analyses models for labyrinth seals.

Experimental Studies on Labyrinth Seals

In 1978, Benckert and Wachter [5] measure the stiffness of labyrinth seals (TOS, ILS, and stepped LS) and investigate the influence of rotor speed and circumferential pre-swirl velocity on seal reaction forces. Their results show that the reaction forces are sensitive to the inlet flow pre-swirl, whereas the influence of rotor speed is minor for a seal with small number of teeth (less than 5). "Swirl webs," a first instance of swirl brakes, could sufficiently reduce the inlet pre-swirl velocity, and accordingly the seal destabilizing forces. Test rotordynamic force coefficients remain approximately constant and are independent of rotor eccentricity to 50% of the seal clearance. The test results support the "eccentricity independent" model discussed in Ref. [6]. Benckert and Wachter find no appreciable difference in the cross-coupled stiffness of an ILS and a TOS LS. Measured stiffness coefficients for a comparatively long ($L/D \rightarrow 1$) LS are negative. Later in 1984, Leong and Brown [7] (1984) report similar results, i.e., most TOR and TOS LSs show a negative direct stiffness; though noting an exception for a short LS ($L/D = 0.1$) with only five cavities.

In 1986, Childs and Scharrer [8] test TOR & TOS labyrinth seals and report their rotordynamic force coefficients. The authors present direct damping coefficients for the first time. The test results show the stiffness and damping coefficients are sensitive to the inlet tangential (swirl) velocity and increase with an increase in inlet pressure. Later, Thieleke and Stetter (1990) [9] point out that the cross-coupled force, arising within each cavity, depends on the change of circumferential velocity from one cavity to the next.

In 1988, Childs et al. [10] measure the leakage and force coefficients for an ILS (C_r = 0.25 mm, average tooth pitch is 5 mm, L/D = 0.34) and a TOS LS (C_r = 0.305 mm, tooth pitch is 4 mm, L/D = 0.30). The authors test the seals at a rotor speed up to 16,000 rpm ($\frac{1}{2}D\Omega$ = 126 m/s) while the supply pressure ranges from 3.0 bar to 8.0 bar ($PR = P_{in}/P_{out}$ = 3.0-8.0). The test results evidence the ILS leaks substantially less (up to 60%) than the conventional TOS LS. Childs et al. note the ILS has frequency dependent rotordynamic force coefficients, which in the 1980s posed a conflict with the generally-held view that force coefficients provide a frequency-independent

[2] Reproduced from Ph.D. proposal of Tingcheng Wu (2018).

relation between reaction forces and rotor displacements. Compared to see-through (TOR and TOS) Ls designs, the ILS usually has a lower and negative cross-coupled stiffness (k). However, a see-through LS shows approximately twice the direct damping coefficient than the corresponding coefficient in an ILS. The direct stiffness coefficient (K) for both configurations is negative; the see-through configuration shows half the magnitude of the direct stiffness for the ILS.

In 1999, Baumann [10] reports a thorough investigation on the effect of labyrinth seals on the stability of high-pressure centrifugal compressors. The units equip with TOS LSs and groove-comb LSs, similar to an ILS or a stepped LS. The author finds that the shop test identified direct stiffness and logarithmic decrement (δ), a measure of viscous damping ($\xi \simeq \delta/2\pi$), for both seal types decrease as the compressor discharge pressure increases. Hence the choice of labyrinth seal affects the compressor system amplification factor and the placement of its critical speed.

In 2007, Paolillo et al. [11] demonstrate the impact of rotor speed on labyrinth seal leakage. The ratio between rotor speed ($U_{rotor} = R\Omega$) and axial flow velocity (W), U_{rotor}/W, plays an important role. When $U_{rotor}/W < 1$, rotor speed has a negligible effect on seal leakage. Li et al. [12] (2011) later confirm this finding through both experimental and numerical analyses. On the other hand, for $U_{rotor}/W > 1$, the seal leakage could significantly decrease. For large velocity ratios $U_{rotor}/W > 5$, the seal leakage decreases more than 20% respect to that at a low velocity ratio conditions [11].

Besides rotor speed, as shown in 2008 by Gamal and Vance [13], the impact of labyrinth seal teeth thickness on seal leakage is also of interest. The authors report that doubling the teeth thickness reduces seal leakage by 10% - 20% for the test seals at all considered supply pressures (P_{in} ranges from 2 bar to 6.9 bar). As the fluid jet leaves the constriction (seal tooth), it expands into the subsequent downstream cavity. Both the clearance and the thickness of the tooth affect the angle of expansion, and therefore the amount of carried over kinetic energy [14]. Therefore, increasing the teeth thickness reduces seal leakage. Also, a thicker bladed seal may increase the frictional loss in the restriction. Test results also evidence that a reduction in cavity depth by up to 80% (the cavity depth ranges from 2.5 mm to 12.7 mm) has virtually no impact on seal leakage. The experimental and numerical analysis results from Li et al. [15] also confirm this finding.

Recall that the frequency dependent characteristic of rotordynamic force coefficients reported by Childs et al. [10] in 1988. Recent test results [16-19] evidence that LSs possess frequency dependent rotordynamic force coefficients; in particular, the direct stiffness coefficient. The test

cross-coupled stiffness is only sensitive to the inlet pre-swirl velocity and not rotor speed. Thus, an inlet pre-swirl rather than rotor speed has a stronger influence on the seal effective damping ratio.

Analyses for Labyrinth Seals

Besides the experimental investigations, theoretical analyses for labyrinth seals are well documented since the early 1900s. In the past, researchers have produced analyses predicting the leakage and rotordynamic force coefficients of labyrinth seals. Notable to this day are the bulk-flow models (BFM) advanced by Vance and Murphy (1980) [20], Kostyuk (1972) [21], Iwatsubo et al. (1980, 1982) [22, 23], and Childs and Scharrer (1986) [24].

A BFM uses film averaged fluid pressure and flow velocities, while the wall shear stress is based on friction factors. Therefore, the BFM predictions strongly depend on the empirical coefficients, i.e., the flow discharge coefficient and the friction factor coefficients. Prior researchers have advanced several friction factor and leakage models to estimate labyrinth seal performance.

In 1908, Martin [25] considers the labyrinth to be a series of discrete throttling processes akin to the flow through a series of orifices. He derives a formula for the leakage flow through a labyrinth seal based on this model using a number of simplifying assumptions.

Later in 1935, Egli [26] examines the effect of changing the number of sharp-edged flow restrictors (teeth) and recommended that Martin's formula be used only when there are four or more throttling restrictors in series. For fewer restrictions, he used the Saint Venant-Wantzel orifice equation for each flow restriction. Egli offers test results for staggered labyrinths which show that the flow coefficient depends on the clearance and thickness of the restrictor. Later, based on Egli's [26] work, Hodkinson [14] (1939) modifies the leakage equation with a semi-empirical expression for the kinetic energy carry-over coefficient.

In 1964, Neumann [27] develops an empirical leakage formula applicable to gases and in contrast to liquids as typical orifice equations does. The formula includes a semi-empirical flow coefficient and a kinetic energy carry-over coefficient. The semi-empirical flow coefficient, accounting for the further contraction of flow after it has passed through the plane of the restrictors (teeth), is a function of the pressure ratio between the upstream and downstream cavities. The kinetic energy carry-over coefficient is determined based on the seal geometry (tooth number,

radial clearance, and the seal length). In labyrinth gas seal BFM predictions, solving the Neumann's leakage equation with an iterative technique gives the leakage through a seal as well as the intermediate seal cavity pressure.

In the bulk-flow model, fluid flow wall shear stresses, an energy dissipation mechanism, are determined in terms of wall friction factors. Therefore, the friction factor plays a prominent role in the rotordynamic force coefficients predictions. Hirs [28] first proposes adopting a Blasius-type pipe friction model ($f = n\mathrm{Re}^m$) in the BFM to evaluate wall friction factors, and from which to calculate the wall surface shear stresses. For smooth surface annular seals, the Blasius friction factor model (n = 0.079, m = -0.25) shows a moderate accuracy against test results [29].

However, for seals with textured surfaces, the Blasius friction model ($f = n\mathrm{Re}^m$) could not accurately estimate textured wall friction factors. Several experiments [30-32] have gathered seals performance and leakage information indicating that the friction factor increases with an increase in seal clearance, thus contradicting the theoretical predictions based on Moody or Blasius friction factor models. In 2000, Al-Qutub et al. [30] develop a new friction factor model for a honeycomb surface as derived from a static seal tester. The friction factor is found to be a function of Reynolds number and seal clearance only. The seal clearance plays a dominant role in this new friction factor model.

Later, through a CFD approach for liquid annular seals with deliberately macro textured surfaces, Villasmil (2002, 2006) [31, 32] finds that within a specific Reynolds number range, the maximum friction factor observed in a specific textured pattern size is independent of the actual clearance, which appears to be related to the cavity length to clearance ratio and the physical cavity size itself. The CFD simulations indicate that textured surface area and its aspect ratios are the parameters defining the friction factor at a given seal clearance. Among those parameters, the surface textured area ratio is the primary parameter defining the flow resistance; a larger surface-textured area ratio leads to more substantial flow resistance (friction factors). The aspect ratio of the textured pattern plays a moderate role once the above-cited ratios are defined. Shallow patterns provide larger friction factors over the deep pattern designs. Besides, the size of the textured pattern relative to the actual clearance also affects the flow resistance.

To evaluate the impact of friction factor on the BFM predictions, D'Souza and Childs [33] (2002) predict the rotordynamic force coefficients of honeycomb gas seals with three variations of the Blasius pipe-friction model: (i) a basic model where the Reynolds number is a linear function

of the local clearance, $f_s = n_s\, Re^{m_s}$ (ii) a model where the coefficient is a function of the local clearance, and (iii) a model where the coefficient and exponent are functions of the local clearance. Their comparisons show that the friction factor model choice is vital in the effective damping coefficient predictions, in particular, at a lower frequency range (60-70 Hz) where industrial centrifugal compressors and steam turbines may become unstable [33]. At higher frequencies, predicted stiffness and damping coefficients tend to deliver identical results for all of the friction models.

Unlike bulk-flow techniques, 3D CFD analysis makes no assumptions on the seal geometry, thus allowing (with a few million nodes) the analysis of fluid flow in an arbitrarily shaped domain, including stepped LSs and ILSs. As commercial software is readily accessible and computers processing speed continuously increase, computational fluid dynamics (CFD) analysis based approaches to solving the Navier-Stokes equations of turbulent flow in seals is (becoming) standard engineering practice.

Once a flow solution is found, integration of the CFD predicted pressure field yields the reaction force acting on the rotor/stator surfaces, therefore leading to the estimation of the rotordynamic force coefficients. Moore [34] reports CFD derived LS predictions showing good correlation with experimental data for both rotordynamic force coefficients and leakage. The authors claim a (marginal) improvement over BFM predictions.

To obtain a seal reaction force, the following experimental methods are common practice: (1) “Pressure” method: assume the axial pressure fluctuations in the cavities are negligible and obtain the force by integrating the measured pressure on the stator (only a few points are needed); (2) “Stator Force” method: utilize a hydraulic shaker to excite the stator and directly measure the force on the stator wall; and (3) “Rotor Force” method: measure the force on the rotor using magnetic bearings (Kwanka [35] and Wagner [36]).

To quantify the influence of the above test methods on the results, Schettel et al. (2005) [37] calculate the rotordynamic force coefficients from CFD predicted flow fields in the way prescribed by each method. The authors present a comparison between experimentally obtained and CFD predicted stiffness coefficients for a comb-grooved labyrinth seal. The test results serve to validate a CFD predicted pressure field. The “Pressure” and “Stator Force” methods do not account for the influence of the up/downstream flow sections, whereas the CFD results show these areas generate a considerable part of the radial force [37]. On the other hand, the “Rotor Force” method integrates

all the pressure field over the whole rotor surface including the up/downstream flow sections. The estimated rotordynamic force coefficients indicate that the stiffness coefficients (*K*, *k*) strongly depends on the method used. Compared to the other two methods, the "Rotor Force" method predicts a significantly lower *K* and higher *k.* Therefore, the impact of the up/downstream flow sections on the rotordynamic force coefficients should also be a concern when designing a new machine [37].

The improvements in the efficiency and power output of turbomachines require optimizations of gas seals. Labyrinth seals, with their simple structure and reliable performance, are preferred. Except for tighter seal clearances, seal configurations are evolving continuously to reduce leakage, e.g., from a see-through design to a stepped labyrinth configurations. Utilizing CFD simulations, Kim et al. [38, 39] analyze the influence of labyrinth seal configurations on leakage behavior in terms the flow function ($\phi = \dot{m}\sqrt{T_{in}}/(A_c P_{in})$, where $\dot{m}$ is the mass flow rate, A_c is the cross section area, T_{in} and P_{in} are the inlet total temperature and pressure, respectively). The see-through labyrinth seal flow function increases with respect to the pressure ratio as well as the radial clearance. However, for a stepped labyrinth seal, an increase in radial clearance yields a more significant flow resistance (pressure loss) for an equivalent flow function [39]. That is, the flow function decreases with an increase in radial clearance. CFD simulations of a stepped labyrinth seal show the leakage is different when flow direction reverses. For a divergent flow arrangement (see Figure 5 (a)), the jet flow out of a clearance hits the next tooth wall more strongly as the clearance increases. On the other hand, for a convergent flow arrangement (see Figure 5 (b)), a larger clearance provides a more abrupt turning of the flow from a tooth tip to the next. Both the above flow fields change lead to a more substantial pressure drop across the tooth tips. Therefore, for a stepped labyrinth seal, the flow function decreases when an increase in seal clearance. A later study by Kang et al. (2010)[40] show that except for the seal teeth configuration, the stepped labyrinth seal leakage considerably depends on the land (rotor) surface structure. For a honeycomb land surface, the flow function decreases with an increase of the clearance to honeycomb width ratio.

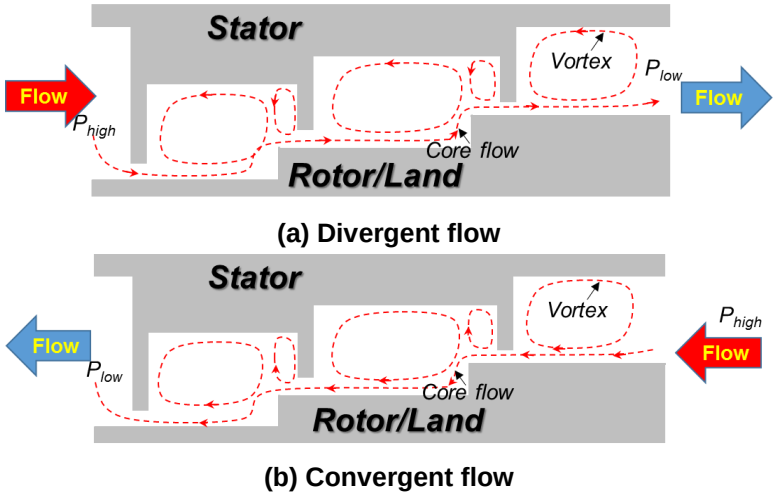

Figure 5. Schematic view of a stepped labyrinth seal: (a) diversion flow direction, and (b) conversion flow direction.

Compared to BFM predictions, CFD solutions deliver details of the flow field, which allows an in-deep knowledge of seal performance. For example, Pugachev et al. [41-43], through CFD predictions of a short comb-grooved seal, find a linear relationship between the stiffness coefficients and inlet swirl force (product of mass flow rate and inlet swirl velocity, $\dot{m} \cdot U_0$). Increasing the clearance from 0.27 mm to 0.5 mm roughly doubles the seal leakage as well as the magnitude of direct stiffness, and halves the cross-coupled stiffness.

In 2013, Gao and Kirk [4] numerically investigate an ILSs with a commercial CFD software and applied a rotating frame transformation to convert the transient state flow (with a whirling rotor) to a steady state one. The authors assume the rotordynamic force coefficients are frequency independent. Unfortunately, prior test results [10] show the rotordynamic force coefficients of the ILs are frequency dependent. Therefore, the obtained CFD predictions may need further validation.

Recently, the rapidly increased computational capacity, as well as the development of advanced algorithms (e.g., Genetic Algorithm), promote research on seal geometry optimization. In 2016, Dai et al. [44] utilize the Genetic Algorithm to identify the optimal configuration of a labyrinth seal. Multiple advanced designs are examined in detail through CFD simulations. In comparison to the baseline geometry (straight tooth see-through labyrinth seal), seals with grooves on the tooth tips show an improvement of 16% in sealing efficiency.

Rai et al. (2016) [45] utilize a 2D CFD analysis to assess the improvement in the leakage performance of a labyrinth seal and propose a new seal configuration with “air-curtains” (air

injection) from the stator. The air-curtains work as fluidic barriers breaking the jet through flow in the seal leakage path. The CFD analysis evidence that implementing air-curtain in the labyrinth seal could reduce leakage by up to 50% of the conventional LS design.

Although the improvement in computational capability, 3D CFD simulations are still time-consuming and computationally expensive when compared to the BFM. For example, Migliorini et al. (2012, 2014) [46, 47] present a new CFD/Bulk-flow hybrid method to determine rotordynamic coefficients of gas seals. Briefly, the authors utilize CFD to determine the steady-state bulk-flow variables (pressure and averaged velocities across the clearance), and a bulk-flow perturbation method to obtain the reaction forces of an eccentric whirling rotor. This hybrid method predictions show better accuracy with experimental results in Ref. [48], as compared to a conventional BFM. With a computation time on the order of a typical bulk-flow analysis, the CFD/BFM hybrid method predicts rotordynamic characteristics comparable to the full 3D transient CFD analysis.

Recently, San Andrés et al. [49] present a CFD modified BFM analysis for circumferentially shallow grooved liquid seals. Integrating the friction factors and the penetration angles in a cavity derived from CFD results into an original BFM, the authors show a significant improvement of the BFM predictions. The BFM predictions show agreement within 14% compared to experimental estimated rotordynamic force coefficients in Ref.[50].

In sum, the bulk-flow model is efficient to model leakage and force coefficients but lacks accuracy due to its multiple simplifications (e.g., the empirical coefficients in the friction factor model), whereas CFD simulations, although requiring more intellectual effort as well as computing time, shows better agreements with test results. Therefore, a modification of the bulk-flow model with CFD derived results could be a practical way to improve the accuracy of the BFM predictions.

3. PREDICTION OF ROTORDYNAMIC FORCE COEFFICIENTS FOR LABYRINTH GAS SEALS

Governing Equations

In 1986, Childs and Scharrer [24], based on Iwatsubo's early model [22, 23], derive the equations of a one control volume bulk flow model applied to a labyrinth seal. The following update follows the original derivation. Figure 6 shows schematic views of an ILS with radial clearance C_r and rotor radius R_s. Teeth on both the rotor and the stator have the same geometry, with B as a tooth height and L_i as a tooth pitch.

The flow domain is divided into n cavities separated by blades. As Figure 7 shows, within the i^{th} cavity, the pressure is $P_{i,}$ and the mean circumferential velocity is U_i. The velocity U_i differs from one cavity to the next, but it is sufficiently uniform in a single cavity to permit its bulk flow representation. The mass flow rate through the upstream and downstream teeth is $\dot{m}_i = \dot{m}_{i+1}$.

The gas density (ρ) follows the ideal gas law, $\rho = P/(Z_g R_g T)$, where R_g and Z_g are the gas constant and compressibility factor, and T is the gas temperature[3]. Figure 8 depicts the forces on a control volume, serving to derive the circumferential momentum equation.

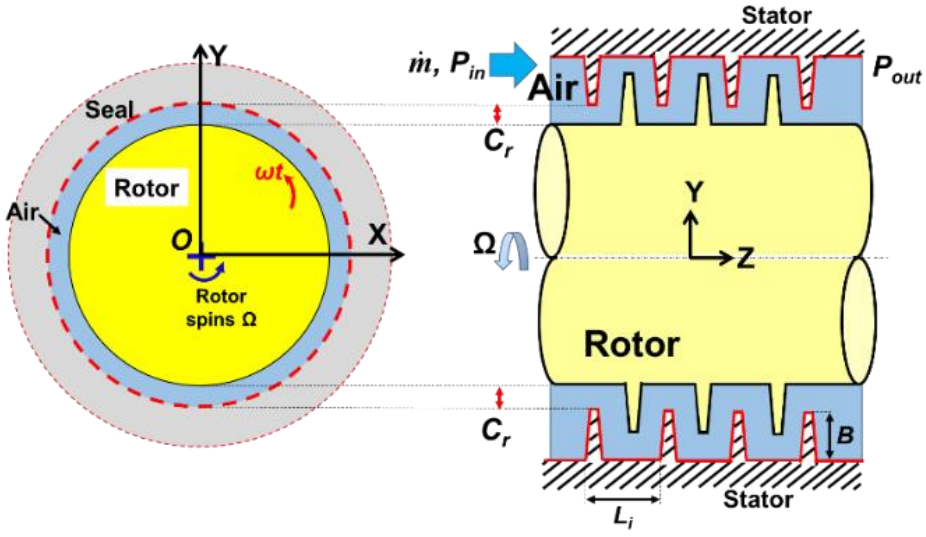

Figure 6. Schematic view (not to scale) of an interlocking labyrinth seal (ILS).

[3] Since experimental investigations do not show a significant temperature change throughout typical seals, the model assumes isothermal flow conditions [5].

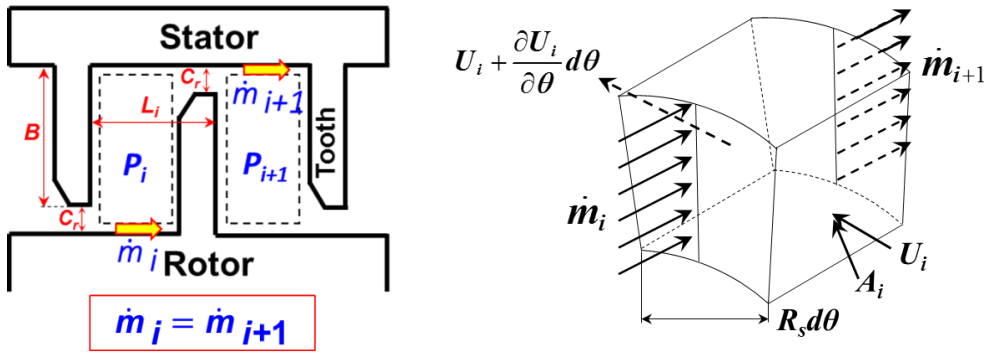

Figure 7. Schematic views of a one-control-volume model (*i* = the cavity number).

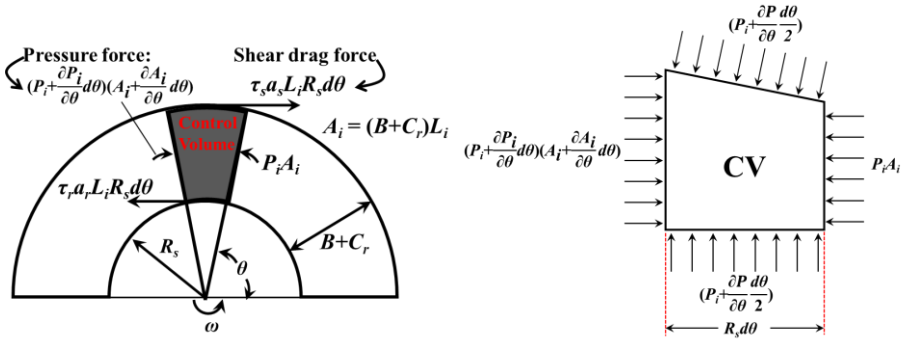

Figure 8. Forces on the control volume of a labyrinth seal (*i* = the cavity number).

In a cavity, the flow mass conservation equation and momentum transport equation along the circumferential (θ) direction are [24]:

$$\frac{\partial(\rho_i A_i)}{\partial t} + \frac{\partial(\rho_i U_i A_i)}{R_s\ \partial\theta} + \bar{\dot{m}}_{i+1} - \bar{\dot{m}}_i = 0 \tag{2}$$

$$\frac{\partial(\rho_i U_i A_i)}{\partial t} + \frac{\partial(\rho_i A_i U_i^{\,2})}{R_s\ \partial\theta} = -\frac{A_i}{R_s}\frac{\partial P_i}{\partial\theta} + (\tau_{r_i} a_{r_i} - \tau_{s_i} a_{s_i}) L_i \tag{3}$$

where $A_i = (B + C_r)L_i$ is the area of a cavity cross-section.

Using Neumann's equation [2] that relates the mass flow rate ($\dot{m}$) through a tooth clearance (C_r) as a function of the upstream (P_{i-1}) and downstream (P_i) cavity pressures,

$$\bar{\dot{m}}_i(\pi D) = \dot{m}_i = \mu_{1i}\mu_{2i}(\pi D C_r)\sqrt{\frac{P_{i-1}^2 - P_i^2}{R_g T}},\ i = 1, 2, \cdots, N \tag{4}$$

where, μ_{1i} is a kinetic energy carry-over coefficient, and μ_{2i} is a flow discharge coefficient, see Ref. [2].

In Eq. (3) a_{r_i} and a_{s_i} are dimensionless lengths introduced in Ref. [6]. For **TOR LS**: $a_{r_i} = (2B + L_i)/L_i$, $a_{s_i} = 1$; **TOS LS**: $a_{r_i} = 1$, $a_{s_i} = (2B + L_i)/L_i$. Since the **ILS** has teeth both on stator and rotor, $a_{r_i} = a_{s_i} = (B + L_i)/L_i$.

The shear stresses τ_{r_i} and τ_{s_i} acting on the rotor and stator, respectively, are defined in terms of friction factors (f_r, f_s) [6]. At the rotor surface,

$$\tau_{r_i} = f_{r_i}\left(\frac{1}{2}\rho_i U_{r_i}^{\,2}\right) = n_r Re_r^{\,m_r}\left(\frac{1}{2}\rho_i U_{r_i}^{\,2}\right) \tag{5.a}$$

where $$U_{ri} = R_s\Omega - U_i,\ Re_r = \frac{\left|R_s\Omega - U_i\right| D_{h_i}}{\nu_i} \tag{5.b}$$

And at the stator surface, $$\tau_{s_i} = f_{s_i}\left(\frac{1}{2}\rho_i U_{s_i}^{\,2}\right) = n_s Re_s^{\,m_s}\left(\frac{1}{2}\rho_i U_{s_i}^{\,2}\right) \tag{6.a}$$

where $$Re_s = \frac{\left|U_i\right| D_{h_i}}{\nu_i},\ U_{s_i} = U_i \tag{6.b}$$

$$D_{h_i} = 2(C_r + B)L_i/(C_r + B + L_i) \approx 2BL_i/(B + L_i) \tag{6.c}$$

where $U_r = \sqrt{W^2 + (U - R\Omega)^2}$ and $U_s = \sqrt{W^2 + U^2}$ are bulk-flow speeds relative to the stator and rotor surfaces, and f_r, f_s are the corresponding friction factors. D_{hi} is the hydraulic diameter, (n_r, m_r) and (n_s, m_s) are empirical coefficients for the Blasius friction model $f = n\ R_e^{\,m}$. In general, for a smooth surface, $n_r = n_s = 0.079$, $m_r = m_s = -0.25$ [6].

The BFM assumes that the shear traction vector is parallel to the direction of the bulk-flow velocity vector. Thus, the wall shear stresses along the circumferential (θ) direction are

$$\tau_{s\theta} = \tau_s\left(\frac{U}{U_s}\right), \quad \tau_{r\theta} = \tau_r\frac{(U - R\Omega)}{U_r} \tag{7}$$

Following Childs and Scharrer [24], subtracting Eqn.(1) times U_i from Eqn.(2) yields the following primitive form of the momentum Eqn. (2):

$$\rho_i A_i\frac{\partial U_i}{\partial t} + \rho_i U_i A_i\frac{\partial U_i}{R_s\partial\theta} + \dot{\bar{m}}_i(U_i - U_{i-1}) = -\frac{A_i}{R_s}\frac{\partial P_i}{\partial\theta} + (\tau_{r_i}a_{r_i} - \tau_{s_i}a_{s_i})L_i \tag{8}$$

Flow Perturbation Analysis

For the i^{th} cavity, the continuity equation (1), circumferential momentum equation (2) and leakage equation (3) are the governing equations for the variables U_i, P_i, and m_i. For small

amplitude rotor motions ($\Delta e_x, \Delta e_y$) of frequency ω, the film thickness (H) as depicted in Figure 9 is

$$H = C_r + e^{j\omega t}(\Delta e_x \cos\theta + \Delta e_y \sin\theta) \tag{9}$$

The velocity and pressure fields are expressed as the sum of a zeroth order and first order complex fields, describing the equilibrium condition and the perturbed motions, i.e.

$$\phi = \phi\{P, U, W\} = \phi_0 + e^{jwt}(\Delta e_x \ \phi_x + \Delta e_y \ \phi_y),\ j = \sqrt{-1} \tag{10}$$

Substitution of the flow variables into the governing equations yields the differential equations for the zeroth and first-order flow fields.

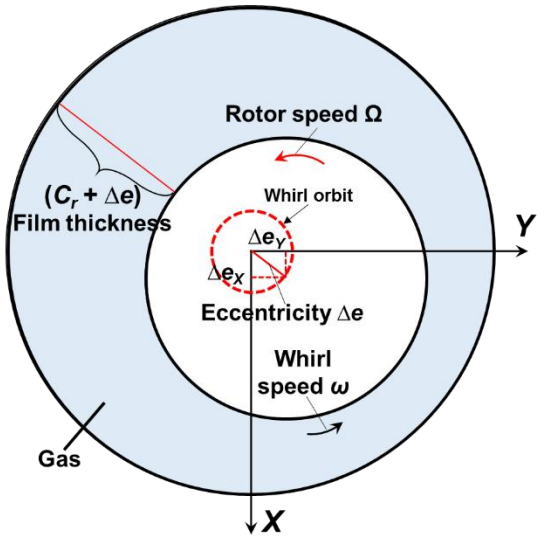

Figure 9. Depiction of small amplitude rotor motions about a centered position.

The zeroth order flow equations

$$\bar{\dot{m}}_0 = \bar{\dot{m}}_i = \bar{\dot{m}}_{i+1}\ ,\ i = 1, 2, 3, \ldots \tag{11}$$

$$\bar{\dot{m}}_0 (U_{0i} - U_{0i-1}) = (\tau_{r0i} a_{r_i} - \tau_{s0i} a_{s_i}) L_i \tag{12}$$

determine the mass flow rate $\dot{m}_0$, cavity pressures (P_{i0}), and velocity field ($U_{i0,}$ i=1,2,..) for the rotor centered position. First-order equations are not detailed for brevity.

Childs [6] details the procedure to solve the partial differential equations governing the fluid flow. The perturbation analysis renders the seal static and dynamic reaction forces as

$$-\begin{bmatrix} F_{X(\omega)} \\ F_{Y(\omega)} \end{bmatrix} = -\begin{bmatrix} F_{X0} \\ F_{Y0} \end{bmatrix} + \begin{bmatrix} D_{(\omega)} & E_{(\omega)} \\ G_{(\omega)} & F_{(\omega)} \end{bmatrix} \begin{bmatrix} X_{(\omega)} \\ Y_{(\omega)} \end{bmatrix} \tag{13}$$

The functions *D-F* are frequency-dependent and obtained as

$$\begin{bmatrix} D \\ G \end{bmatrix}_{(\omega)} = R_s \int_0^L \int_0^{2\pi} P_X \begin{bmatrix} \cos\theta \\ \sin\theta \end{bmatrix} d\theta\, dz; \begin{bmatrix} E \\ F \end{bmatrix}_{(\omega)} = R_s \int_0^L \int_0^{2\pi} P_Y \begin{bmatrix} \cos\theta \\ \sin\theta \end{bmatrix} d\theta\, dz \tag{14}$$

Note that for motions about a centered rotor position, $D = F$, $E = -G$. Stiffness and damping coefficients follow from

$$K_{(\omega)} + j\,\omega C_{(\omega)} \leftarrow D_{(\omega)};\; k_{(\omega)} + j\,\omega c_{(\omega)} \leftarrow E_{(\omega)} \tag{15}$$

The BFM analysis procedure is well documented in Refs. [6, 24, 51]. In brief, the BFM solution procedure follows the steps:

(1) Determine whether the flow is choked or not by comparing the inlet pressure against the critical inlet pressure (as discussed later);

(2) Calculate the mass flow rate, cavity pressure distribution and the cavity circumferential velocity.

(3) Solve the first order (perturbed) equations for a given whirl frequency (ω), integrate the dynamic pressure acting on the rotor surface to calculate the reaction forces, and thus obtaining the rotordynamic force coefficients.

4. CFD ANALYSIS PROCEDURE

Predictions of rotordynamic force coefficients using a BFM strongly depend on the wall friction factors as well as the leakage (Neumann's) equation. Prior investigations evidence the friction factor is a function of the seal operating conditions and the seal geometry. The Blasius friction model currently used in the BFM is only a function of the Reynolds number ($f = n\,\mathrm{Re}^m$, typically $n = 0.079$, and $m = -0.25$).

The momentum Eqn. (3) shows that only the circumferential direction friction factors ($f_{r\theta}$, $f_{s\theta}$) are of interest in the BFM. Therefore, only $f_{r\theta}$ and $f_{s\theta}$ are quantified in this work. The TOS seal geometry and its operating conditions applied in this work are based on a TOS labyrinth seal tested by Vannini et al. (2014) [52].

Table 1 details the TOS labyrinth seal geometry and operating parameters. Figure 10 shows a schematic view of the TOS labyrinth seal, having 14 teeth on the stator. The teeth are equally distributed with pitch length L_i of 5 mm. To investigate the effect of seal geometry and operating conditions on the friction factors, the seal clearance varies[4] from $0.8C_r$ to $1.2C_r$for the three types

[4] The radial clearance C_r varies ±20% in this work. A larger change in radial clearance, up to $2C_r$, is recommended for a later study.

of LS. Similarly, perturbations also apply to the seal operating conditions. For all TOS labyrinth seals (various radial clearances), the rotor speed ranges from 7,000 rpm to 15,000 rpm. Air enters the seal with supply pressure P_{in} = 60, 73, 100 bar (absolute) and room temperature (27 ^{o}C). The seal outlet the exit pressure (P_{out}) is set to determine a pressure ratio ($PR = P_{out}/P_{in}$) ranging from 0.4 to 0.85.

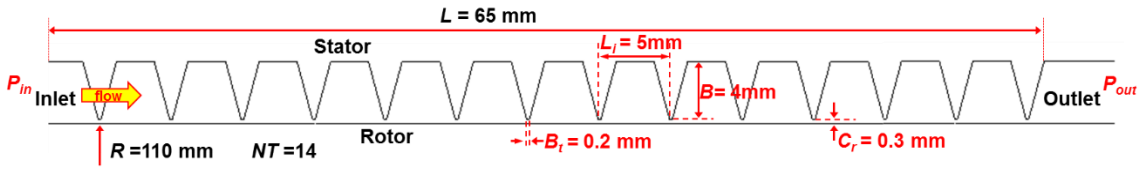

Figure 10. Schematic view of TOS labyrinth gas seal in Ref. [52].

Table 1. Dimensions and operating conditions of the teeth-on-stator (TOS) labyrinth seal in Ref. [52].

Seal Geometry	Seal length, L	65 mm
	Rotor diameter, D	220 mm
	Radial clearance, C_r	0.3 mm
	Teeth number, NT	14
	Tooth pitch, L_i	5 mm
	Height, B	4 mm
	Width at tip, b_t	0.2 mm
Air Properties (ideal gas)	Density, ρ @13bar	15.1 kg/m^3
	Temperature, T	300 K
	Sound speed, V_s	314 m/s
	Viscosity, v	1.51×10^{-5} m^2/s
Operating Conditions	Supply pressure, P_{in}	60 bar ~ 100 bar
	Pressure ratio, $PR = P_{out}/P_{in}$	0.40 ~ 0.85
	Pre-swirl velocity, U_0	0 ~ 0.72 $R\Omega$
	Rotor Speed, Ω ($R\Omega$)	5-15 krpm (58 ~173 m/s)

Figure 11 shows the computational domain and corresponding mesh for the TOS labyrinth seal with nominal radial clearance. 15 mm in length extensions at the seal upstream and downstream flow sections capture the flow field before and after the seal section, respectively. Various mesh sets, their total node count ranging from 2.8 million to 10 million, serve to conduct a mesh independence analysis, see Table 2. The grid independence analysis is not discussed here for simplicity. The grid independence test indicates a mesh with 8.7 million nodes is sufficient to capture the flow field characteristics.

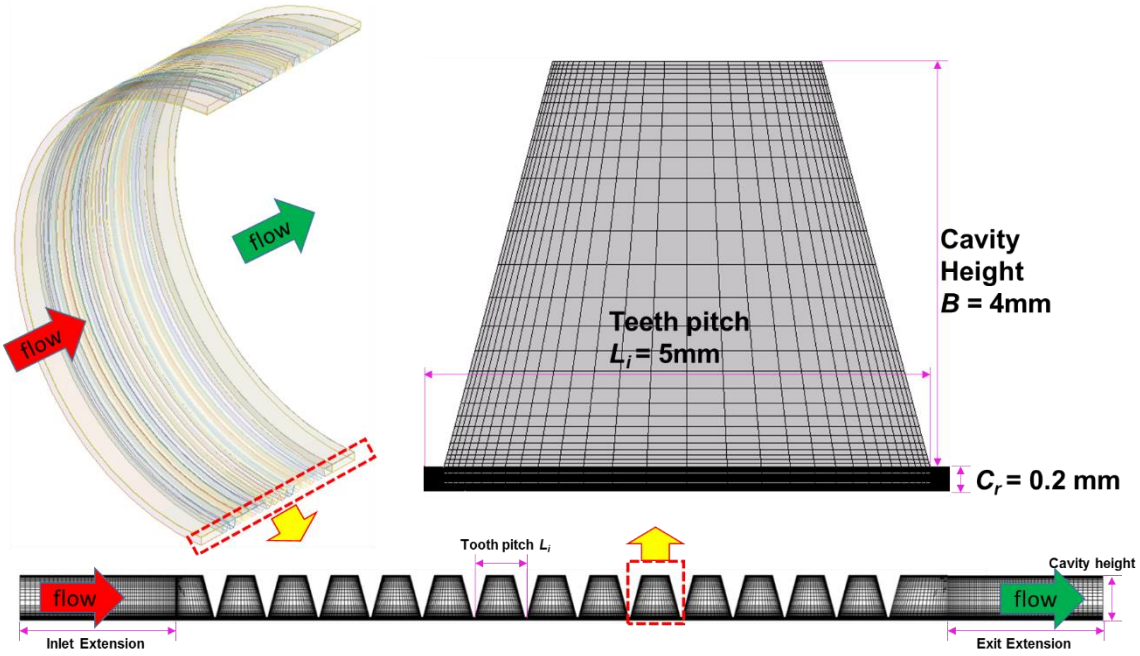

Figure 11. CFD mesh for a TOS labyrinth gas seal.

Table 2. Details of mesh distribution for model labyrinth seals.

	Node number/ mesh size
Radial clearance	30
Tooth section	30
Cavity depth/length	30
Circumferential	180 (2° apart)
Min. mesh orthogonal quality	0.99

5. CFD DERIVED FRICTION FACTORS

Recall the circumferential wall friction factors ($f_{r\theta} = n_r Re^{mr}$, $f_{s\theta} = n_s Re^{ms}$) are functions of the circumferential Reynolds numbers,

$$Re_{r\theta} = \rho\left(U - R\Omega\right) D_h / \mu \tag{16.a}$$

$$Re_{s\theta} = \rho U D_h / \mu \tag{16.b}$$

For a compressible fluid, the density (ρ) is a function of the local pressure, thus varying from cavity to cavity. From the seal inlet plane towards the outlet plane, the circumferential flow velocity develops. Recall, the BFM assumes the cavity pressure (and density), and the circumferential velocity are constant within a cavity. Therefore, all the above variables extracted from CFD results for a friction factor analysis should correspond to the width and radial depth across film average values of a whole cavity.

Figure 12(a) shows the contours of density along the seal. The density within a cavity (#1-#13) is almost uniform; and so does the tangential velocity in a cavity. Figure 12(c) and (d) depict the average (normalized) density (ρ/ρ_s) and the average (normalized) circumferential velocity (U/U_{rotor}, $U_{rotor} = R\Omega$) from the seal inlet plane to the outlet plane.

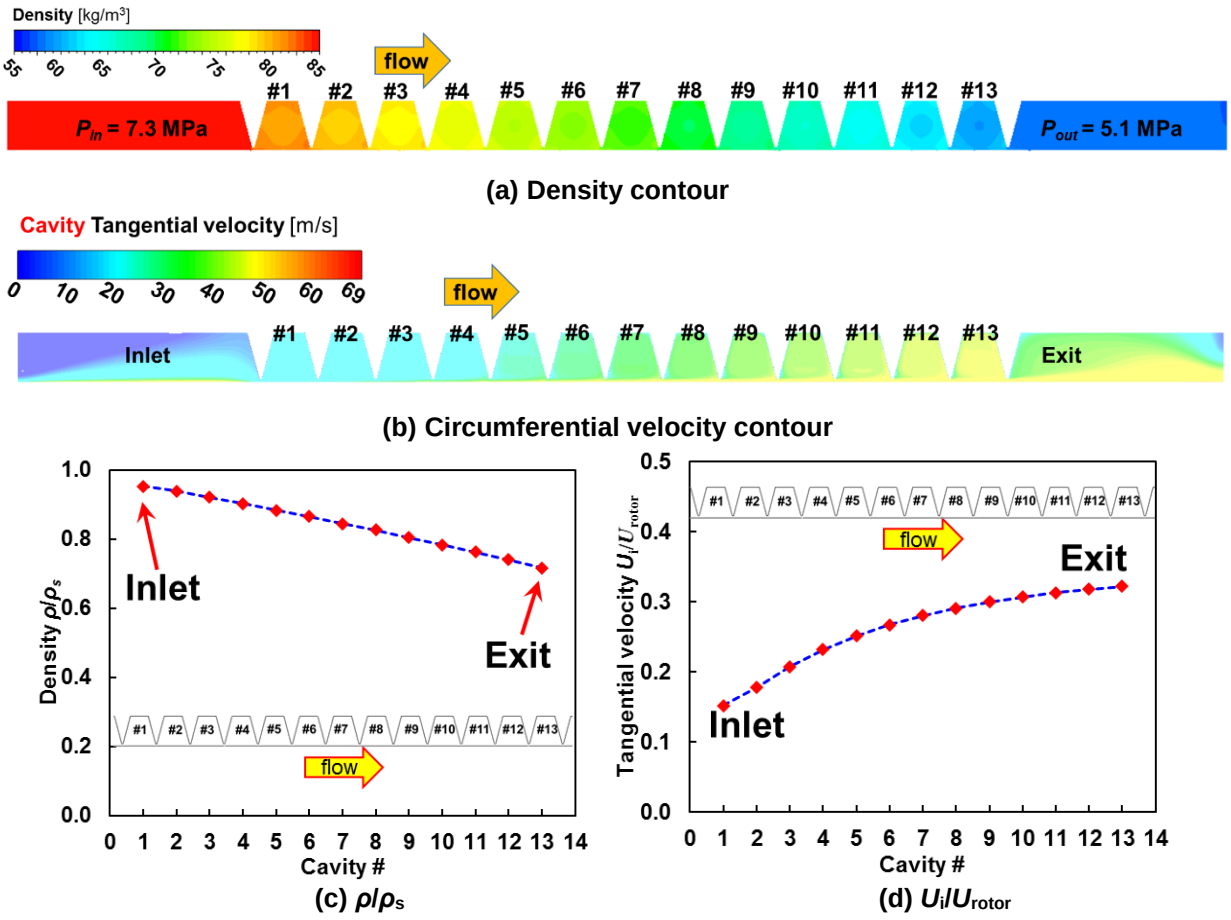

Figure 12. CFD predictions for a TOS LS: (a) density contours; (b) circumferential velocity contours; (c) averaged cavity density (ρ/ρ_s); (d) averaged cavity tangential velocity (U_i/U_{rotor}). P_{in} = 7.3 MPa, P_{out} = 5.1 MPa, rotor speed = 12 krpm (138 m/s).

5.1 Effect of Radial Clearance (C_r) on Friction Factor f_θ

Figure 13 shows the wall shear stresses, $\tau_{r\theta}$ and $\tau_{s\theta}$ on the rotor and stator surfaces, along the axial direction for three radial clearances (C_r). The CFD predictions show $\tau_{r\theta} \gg \tau_{s\theta}$, a larger drag torque on the rotor surface than on the stator. An increase in radial clearance, from 0.8 C_r to 1.2 C_r, increases the rotor surface shear stress ($\tau_{r\theta}$); whereas the stator surface shear stress ($\tau_{s\theta}$) decreases.

Figure 14 depicts the average cavity circumferential velocity (U_i/U_{rotor}) as well as the cavity density (ρ/ρ_s) versus axial length for three clearances, (0.8, 1, 1.2)×C_r. The circumferential velocity evolves from the seal entrance section towards its exit plane. As expected, the cavity circumferential velocity U decreases for a seal with a large radial clearance (1.2C_r). Interestingly, the CFD results indicate the static pressure (P) distribution does not change with clearance (C_r). Therefore, the cavity density ($\rho \sim P$) distribution remains the same in spite of the change in radial clearance.

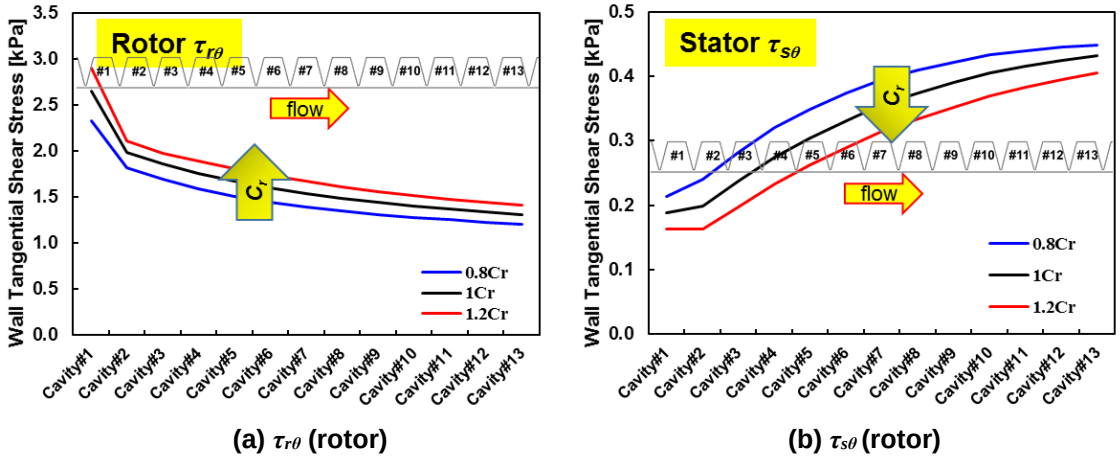

(a) $\tau_{r\theta}$ (rotor) (b) $\tau_{s\theta}$ (rotor)

Figure 13. Wall shear stresses $\tau_{r\theta}$ and $\tau_{s\theta}$ vs. cavity # for three radial clearances (0.8, 1, 1.2)×C_r: (a) rotor surface $\tau_{r\theta}$; (b) stator surface $\tau_{s\theta}$. TOS LS: P_{in} = 7.3 MPa, P_{out} = 5.1 MPa, rotor speed = 12 krpm.

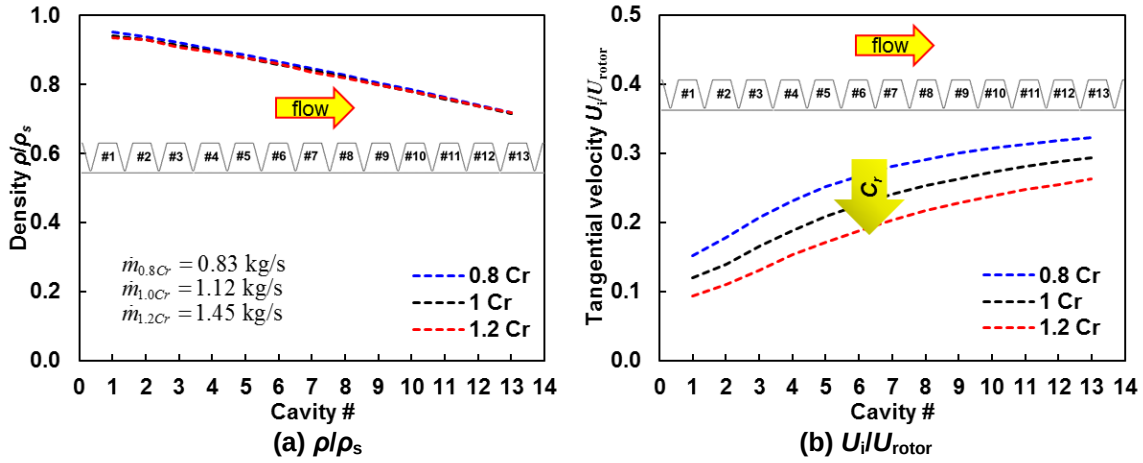

(a) ρ/ρ_s (b) U_i/U_{rotor}

Figure 14. Cavity Circumferential velocity U_i/U_{rotor} and density ρ/ρ_s vs. cavity number for three radial clearances (0.8, 1, 1.2)×C_r. TOS LS: P_{in} = 7.3 MPa, P_{out} = 5.1 MPa, rotor speed = 12 krpm.

Recall Eqn. (5), the relation between the wall shear stresses ($\tau_{r\theta}$, $\tau_{s\theta}$) and the wall friction factor ($f_{r\theta}$, $f_{s\theta}$); hence, with the above flow parameters extracted from CFD results, one could derive the wall friction factor at each cavity. Figure 15 shows the derived wall friction factors $f_{r\theta}$ and $f_{s\theta}$ at

operating conditions with respect to changes in radial clearance. Figure 15 (a) and (b) shows the friction factors when the seal operates at P_{in} = 7.3 MPa and P_{out} = 5.1 MPa, while those in Figure 15 (c) and (d) are obtained at P_{in} = 10 MPa and P_{out} = 4 MPa. Though the rotor surface has larger drag torque ($\tau_{r\theta}$), considering the difference in relative tangential velocity U_{ri} and U_{si}, the CFD delivers $f_{r\theta} \ll f_{s\theta}$. Notably, the rotor surface wall friction factor ($f_{r\theta}$) remains unchanged as the radial clearance increases from $0.8C_r$ to $1.2C_r$. On the other hand, increasing the radial clearance (C_r) promotes the stator surface friction factor ($f_{s\theta}$). $f_{s\theta}$ increases ~ 25% when the radial clearance changes from 0.8 C_r to 1 C_r or from 1 C_r to 1.2 C_r.

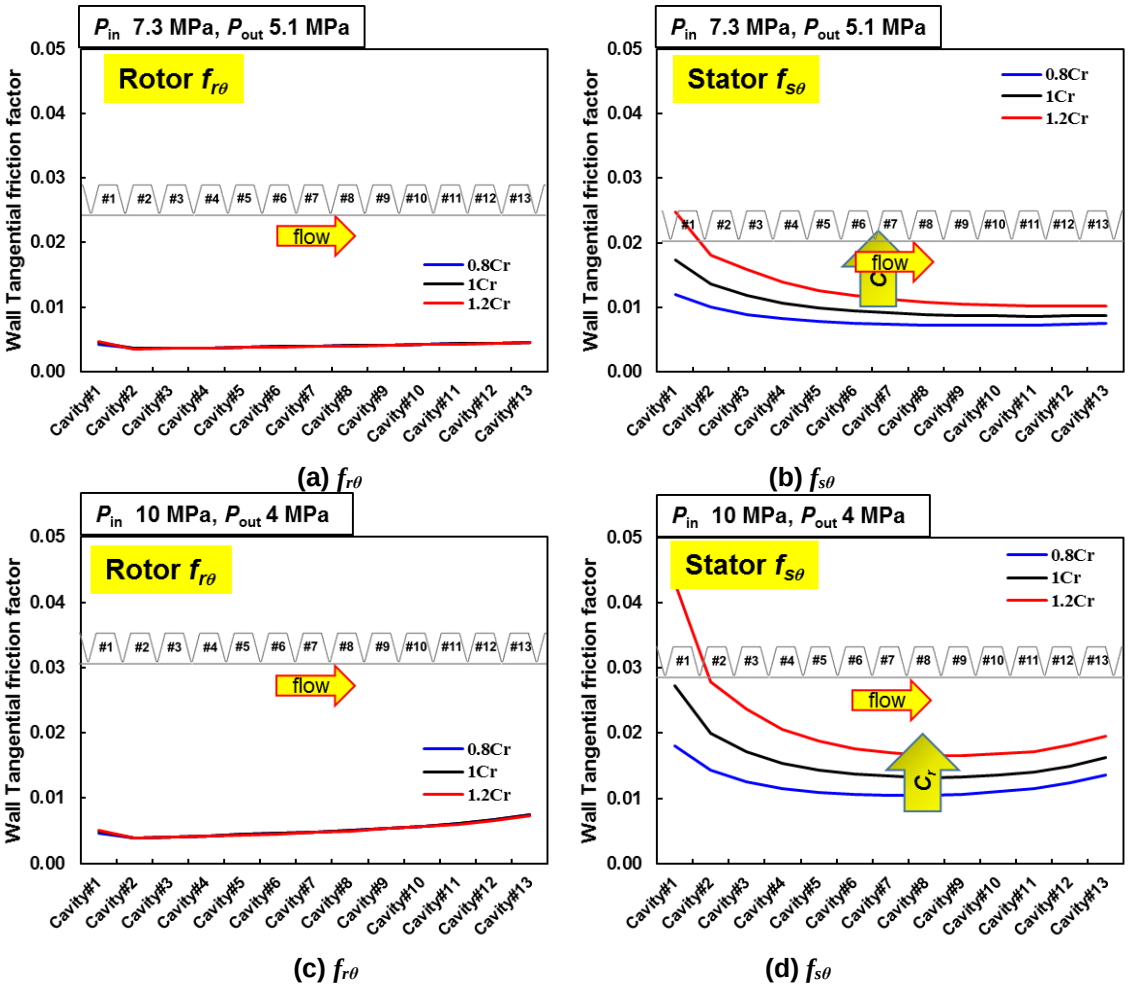

Figure 15. CFD derived friction factors $f_{r\theta}$, $f_{s\theta}$ vs. cavity number for three radial clearances (0.8, 1, 1.2)×C_r. TOS LS: (a) and (b) P_{in} = 7.3 MPa, P_{out} = 5.1 MPa; (c) and (d) P_{in} = 10 MPa, P_{out} = 4 MPa. Rotor speed = 12 krpm.

Figure 16 shows $f_{r\theta}$ and $f_{s\theta}$ from both CFD (friction factor not cavity averaged) and the Blasius friction factor model (f = 0.079 $Re^{-0.25}$) vs. seal axial length. The Blasius friction model is based on the CFD predicted cavity density (ρ) and tangential velocity (U). Note the CFD Reynolds

number Re_r ranges from 1.5 ×10^6 to 2.5 ×10^6, and Re_s from 3.3 ×10^5 to 6.3 ×10^5. The CFD $f_{r\theta}$ << $f_{s\theta}$ and varies slightly within a cavity. On the other hand, $f_{s\theta}$ shows a large variation in a cavity as the local velocity suddenly changes near a stator wall. The Blasius friction factor model underestimates both $f_{r\theta}$ and $f_{r\theta}$ when compared to those predicted via CFD.

A Blasius friction factor model with new coefficients listed in Table 3 shows better agreement with the CFD predictions. The CFD obtained friction factor coefficients n_r is ~ twice the classical one (n = 0.079). When C_r varies by ±20%, n_r is constant while n_s varies ±25%. Notably, the stator surface friction factor is significantly underestimated by the classical friction factor model (n = 0.079, m = -0.25). The CFD derived n_s is thrice the typical magnitude.

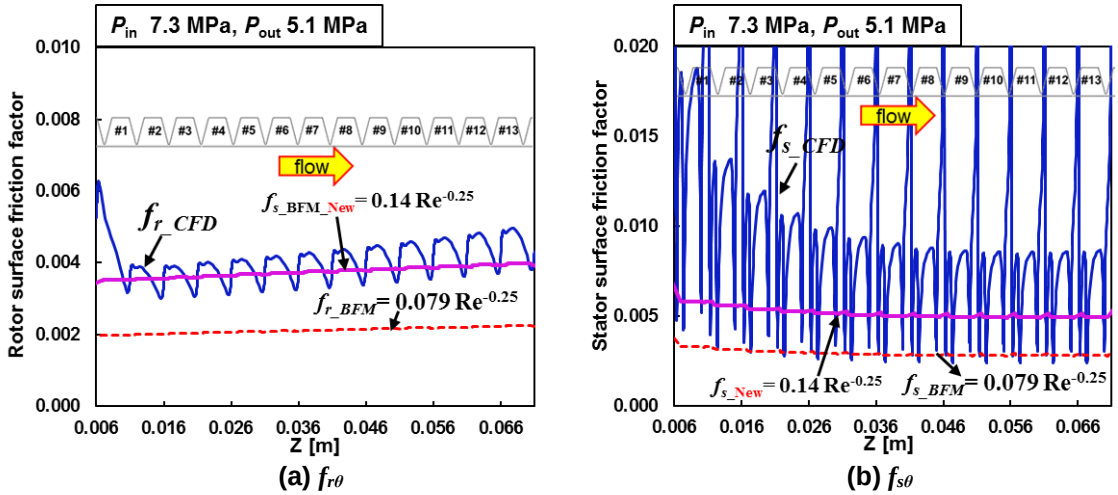

Figure 16. BFM derived friction factors ($f_{r\theta}$, $f_{s\theta}$) and CFD predicted friction factor ($f_{r\theta}$, $f_{s\theta}$) vs. axial length. TOS LS (1C_r): P_{in} = 7.3 MPa, P_{out} = 5.1 MPa, rotor speed = 12 krpm. f's with new (n, m) coefficients included.

Table 3. New friction factor coefficients (n, m) obtained for three clearances.

C_r	n_r	m_r	n_s	m_s
0.8	0.14		0.23	
1	0.14	-0.25	0.28	-0.25
1.2	0.14		0.35	

5.2 Effect of Rotor Speed (Ω) on Friction Factor f_θ

Figure 17 shows the wall shear stresses $\tau_{r\theta}$ and $\tau_{s\theta}$ for operation at four rotor speeds ($R\Omega$ = 58 m/s to 173 m/s, Re_r = 6.6 ×10^5 to 3.1 ×10^6, and Re_s = 1.2 ×10^5 to 6.4 ×10^5). The radial clearance is set as 1C_r. Rotor speed enhances both $\tau_{r\theta}$ and $\tau_{s\theta}$. On the other hand, $\tau_{r\theta} \gg \tau_{s\theta}$ due to a higher shear drag on the rotor surface. Figure 17 (c) shows $\tau_{r\theta}/(R\Omega)$, the rotor tangential wall shear stress per

unit circumferential velocity presents a negligible change with respect to an increase in rotor speed Ω (except in the region close to the seal entrance).

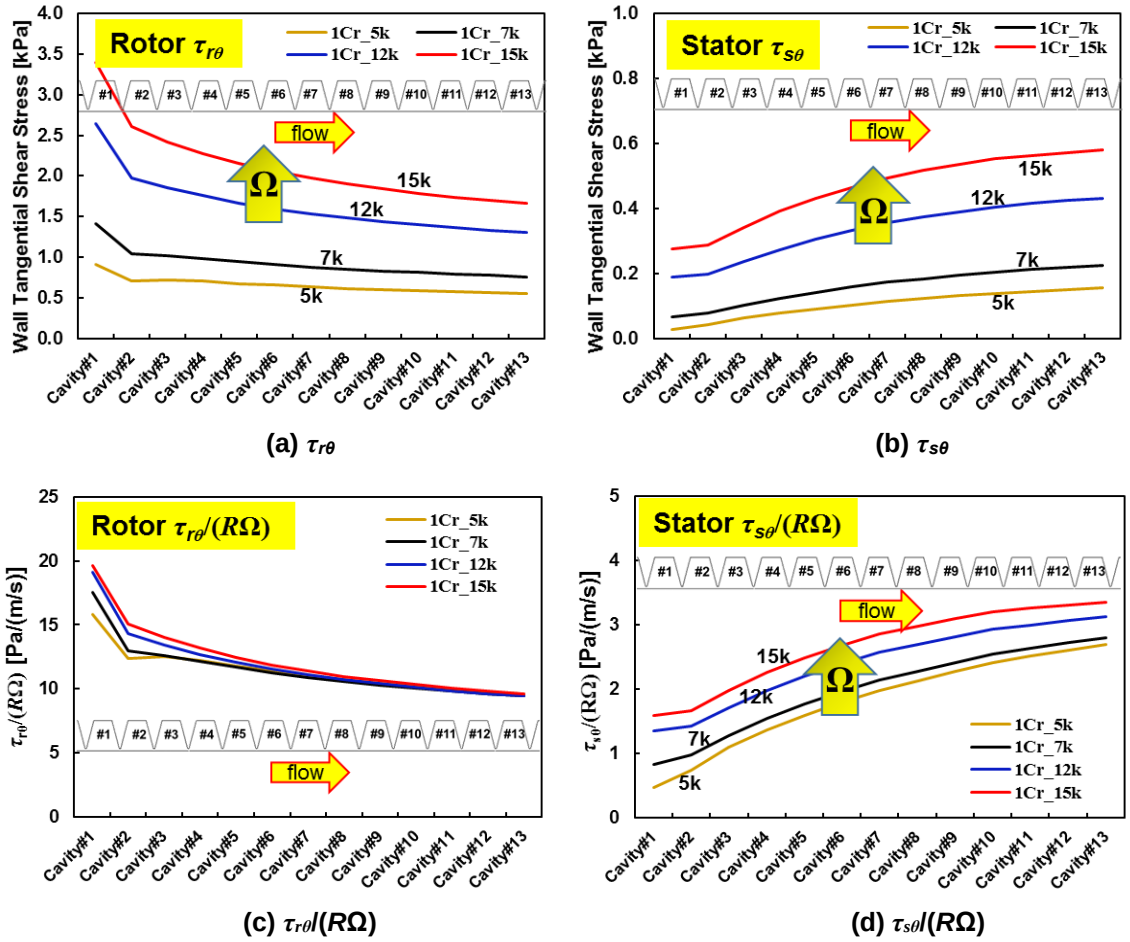

Figure 17. Wall shear stresses $\tau_{r\theta}$ and $\tau_{s\theta}$ vs. cavity number for operation at four rotor speeds Ω = (5, 7, 12, 15)×krpm: (a) rotor surface $\tau_{r\theta}$; (b) stator surface $\tau_{s\theta}$; (c) rotor surface $\tau_{r\theta}/(R\Omega)$; (d) stator surface $\tau_{s\theta}/(R\Omega)$. TOS LS (1C$_r$): P_{in} = 7.3 MPa, P_{out} = 5.1 MPa.

Figure 18 depicts the cavity circumferential velocity $U_i/(R\Omega)$ and density (ρ_i/ρ_s). The circumferential velocity increases with rotor speed, whereas the cavity density (or pressure) retains the same magnitude regardless of a rotor speed change, see Figure 18 (b). This shows rotor speed does not affect LS leakage, as is well known.

Recall the wall friction factors ($f_{r\theta} = 2\tau_{r\theta}/\rho(U - R\Omega)^2$, $f_{s\theta} = 2\tau_{s\theta}/\rho U^2$) are functions of the wall shear stress and cavity relative velocity. The increase in rotor speed promotes both $\tau_{r\theta}$ and $\tau_{s\theta}$ and U_i. Thus, Figure 19 demonstrates the effect of rotor speed on the wall friction factors $f_{r\theta}$ and $f_{s\theta}$. One should notice the scale difference as $f_{r\theta} \ll f_{s\theta}$. The CFD predicted $f_{r\theta}$ and $f_{s\theta}$ decrease with respect to an increase in rotor speed, and so do too $f_{r\theta}/(R\Omega)$ and $f_{s\theta}/(R\Omega)$.

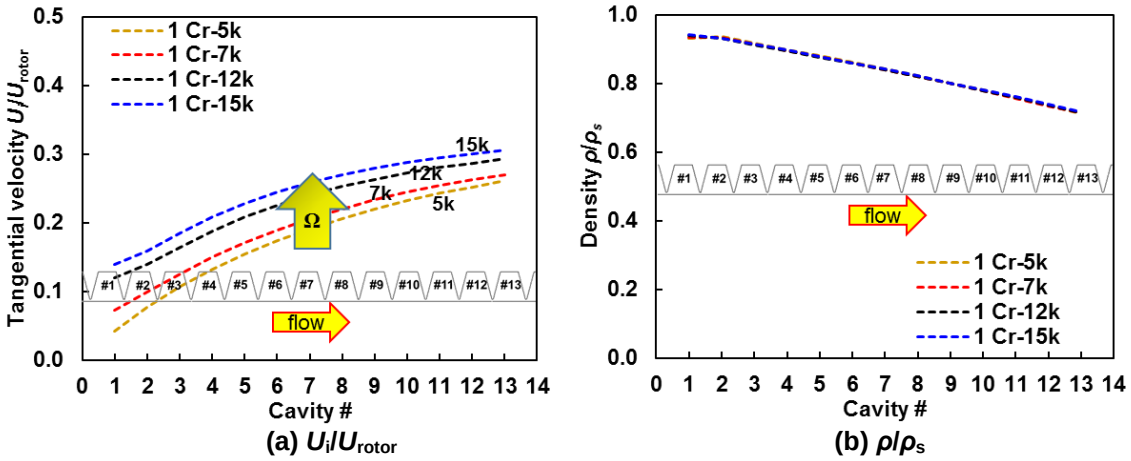

(a) U_i/U_{rotor} (b) ρ/ρ_s

Figure 18. Seal circumferential velocity U_i/U_{rotor} and density ρ/ρ_s vs. cavity number for operation at four rotor speeds Ω = (5, 7, 12, 15)×krpm. TOS LS: P_{in} = 7.3 MPa, P_{out} = 5.1 MPa.

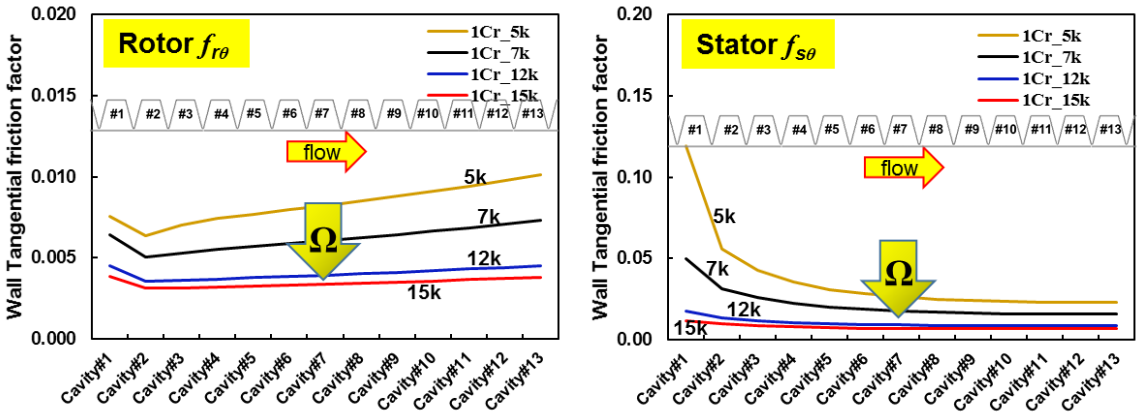

(a) $f_{r\theta}$ (b) $f_{s\theta}$

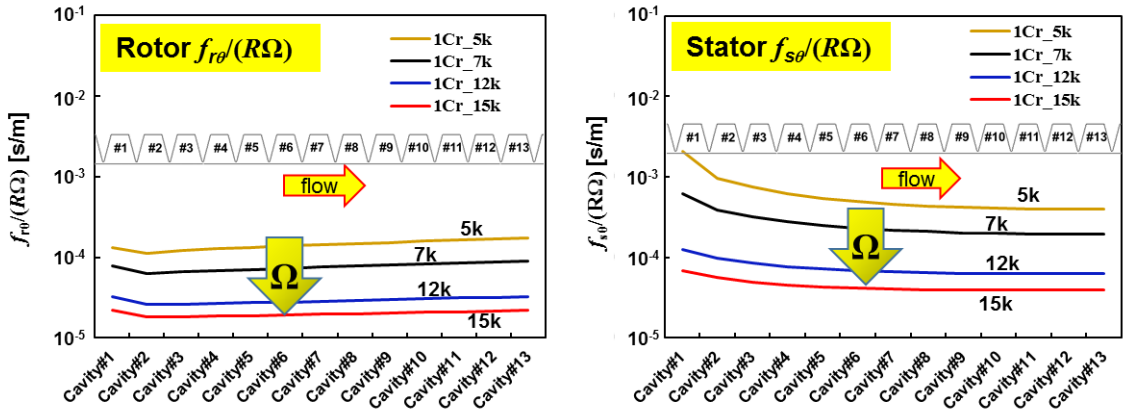

(c) $f_{r\theta}/(R\Omega)$ (d) $f_{s\theta}/(R\Omega)$

Figure 19. Friction factors ($f_{r\theta}$, $f_{s\theta}$,) and ($f_{r\theta}$, $f_{s\theta}$)/($R\Omega$) vs. cavity number for operation at four rotor speeds Ω = (5, 7, 12, 15)×krpm. TOS LS (1C_r): P_{in} = 7.3 MPa, P_{out} = 5.1 MPa.

Table 4 lists the new friction factor coefficients (n, m) for four rotor speeds. The CFD obtained friction factor coefficients (n, m) are quite large (up to 9 times) than the classical ones (n = 0.079, m = -0.25), particularly when the seal operates at a low rotor speed.

Table 4. New friction factor coefficients (n, m) obtained for four rotor speeds.

Ω (krpm)	$R\Omega$ (m/s)	n_r	m_r	n_s	m_s
5	58	0.25	-0.25	0.70	-0.25
7	81	0.20		0.48	
12	138	0.14		0.28	
15	173	0.13		0.23	

5.3 Effect of Pressure Ratio ($PR = P_{out}/P_{in}$) on Friction Factor f_θ

The pressure ratio $PR = (P_{out}/P_{in})$ is a critical parameter for LS leakage and rotordynamic force coefficients. Figure 20 depicts rotor and stator wall shear stresses, $\tau_{r\theta}$ and $\tau_{s\theta}$, for various supply pressures (in the legend, P stands for the supply pressure in bar). Changes in the supply pressure P_{in} and the discharge pressure P_{out} establish pressure ratios ranging from 0.4 to 0.85. As Figure 20 shows, when the supply pressure P_{in} is fixed, the wall shear stresses ($\tau_{r\theta}$, $\tau_{s\theta}$) decrease with respect to an increase in the pressure ratio PR (or the discharge pressure P_{out}). On the other hand, when PR is fixed, an increase in the supply pressure results in larger wall shear stresses $\tau_{r\theta}$ and $\tau_{s\theta}$.

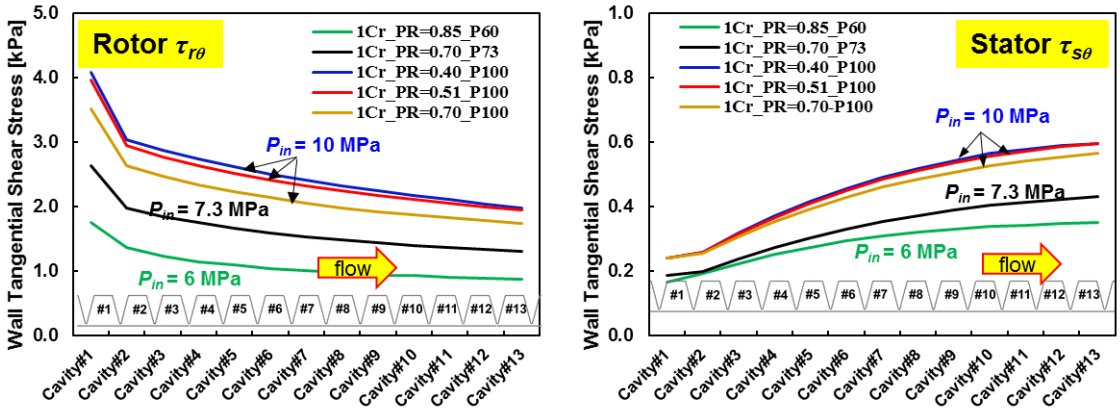

(a) $\tau_{r\theta}$ **(b) $\tau_{s\theta}$**

Figure 20. Wall shear stresses $\tau_{r\theta}$ and $\tau_{s\theta}$ vs. cavity number for operation at four pressure ratios PR = 0.40-0.85. TOS LS (1C$_r$): rotor speed = 12 krpm, P_{in} and P_{out} vary.

Figure 21 (a) shows the average cavity circumferential velocity $U_i/(R\Omega)$ and density (ρ_i/ρ_s) vs. cavity number for various pressure ratios, PR. As the PR increases from 0.40 to 0.85, both the cavity circumferential velocity $U_i/(R\Omega)$ and density ρ_i/ρ_s increase. Notably, when the pressure ratio (PR) is fixed, the circumferential velocity $U_i/(R\Omega)$ as well as (ρ_i/ρ_s) remains the same regardless

of the changes in the supply or discharge pressure (P_{in} or P_{out}). On the other hand, as the cavity density ρ_i is a function of the local pressure, (ρ_i/ρ_s) increases with a larger discharge pressure (larger *PR*), see Figure 21 (b).

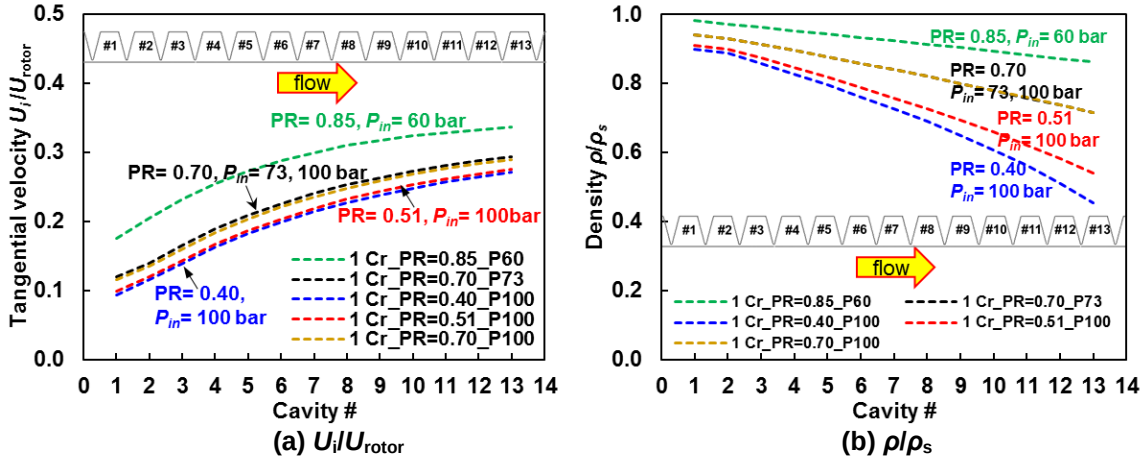

Figure 21. Circumferential velocity U_i/U_{rotor} and density ρ/ρ_s vs. cavity number for operation at four pressure ratios *PR* = 0.40-0.85. TOS LS: rotor speed = 12 krpm, P_{in} and P_{out} vary.

Figure 22 shows the rotor and stator circumferential friction factors, $f_{r\theta}$ and $f_{s\theta}$, for distinct variations in pressure ratios (*PR*). As the supply pressure P_{in} increases from 6.3 MPa (63 bar) to 10 MPa (100 bar), and the discharge pressure varies from 4 MPa to 7 MPa, the pressure ratio *PR* ranges from 0.40 to 0.85. CFD results indicate that the friction factors ($f_{r\theta}$, $f_{s\theta}$) are sensitive to an increase in *PR*. An increase in *PR* results in a lower circumferential friction factor for both the rotor and the stator surfaces. When the pressure ratio (*PR*) is fixed, the friction factors ($f_{r\theta}$ and $f_{s\theta}$) remain the same regardless of the variations in the supply or discharge pressure (P_{in} or P_{out}). Table 5 lists the new friction factor coefficients (*n*, *m*) for four pressure ratios.

The CFD obtained friction factor coefficients (*n*, *m*) are larger than those of the classical model (*n* = 0.079, *m* = -0.25), particularly on the stator surface. At a low pressure ratio condition, the CFD predicted *f* is up to 5 times higher than the classical Blasius *f* estimation.

Table 5. New friction factor coefficients (*n*, *m*) obtained for four pressure ratios.

PR	P_{in} (bar)	n_r	m_r	n_s	m_s
0.40	100	0.20	-0.25	0.43	-0.25
0.51	100	0.18		0.38	
0.70	73, 100	0.14		0.28	
0.85	60	0.12		0.17	

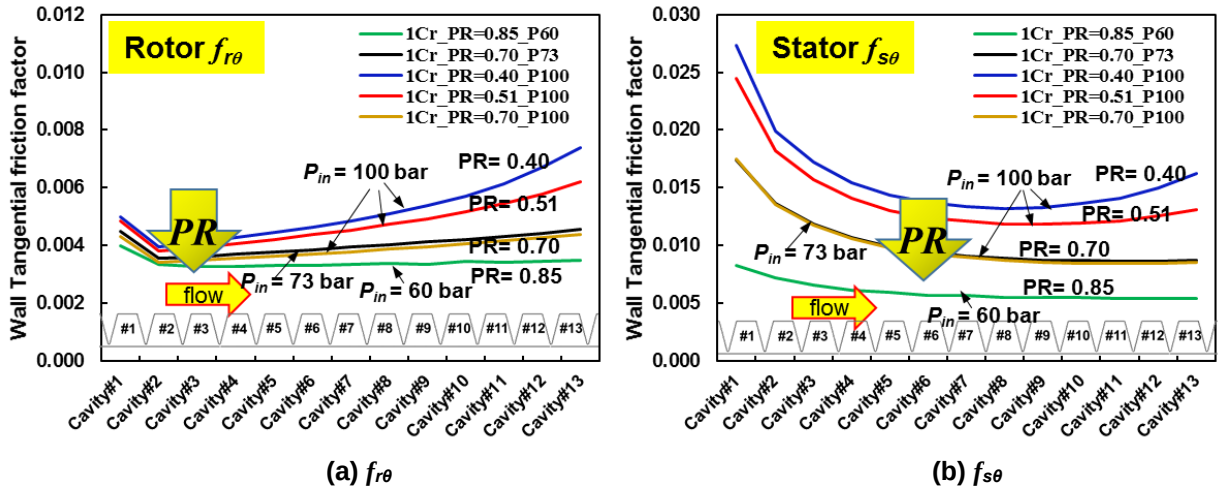

(a) $f_{r\theta}$ (b) $f_{s\theta}$

Figure 22. Friction factors $f_{r\theta}$ and $f_{s\theta}$ vs. cavity number for operation at four pressure ratios *PR* = 0.40-0.85. TOS LS (1C$_r$): rotor speed = 12 krpm, P_{in} and P_{out} vary.

5.4 Effect of Pre-Swirl Velocity Ratio ($\alpha = U_0/R\Omega$) on Friction Factor f_θ

Prior research has evidenced that the inlet pre-swirl velocity ratio $\alpha = U_0/(R\Omega)$ has a significant impact on the cross-coupled stiffness of a labyrinth seal. Figure 23 and Figure 24 illustrate the effect of the inlet pre-swirl velocity ratio (α) on the wall shear stresses $\tau_{r\theta}$ and $\tau_{s\theta}$, the cavity circumferential velocity $U_i/(R\Omega)$, and the cavity density (ρ_i/ρ_s). With an increase in α, the difference between $\tau_{r\theta}$ and $\tau_{s\theta}$ becomes smaller and smaller. Generally, when the pre-swirl ratio (α) increases, the rotor wall shear stress $\tau_{r\theta}$ decreases, and the stator wall shear stress $\tau_{s\theta}$ increases. As expected, a larger pre-swirl velocity promotes a larger cavity average circumferential velocity, see Figure 24(a). As Figure 24(b) depicts, the CFD results show a negligible impact of the circumferential pre-swirl velocity on the seal cavity density (or pressure) distribution.

Figure 25 depicts the wall friction factors $f_{r\theta}$ and $f_{s\theta}$ for four pre-swirl ratios (α). Interestingly, the rotor wall friction factor $f_{r\theta}$ is quite similar for operation with pre-swirl ratios (α) ranging from 0.42 to 0.72. On the other hand, the stator surface friction factor $f_{s\theta}$ decreases as α increases from 0.42 to 0.72.

Table 6 lists the new friction factor coefficients (n, m) obtained for four inlet pre-swirl ratios. The CFD obtained friction factor coefficients n_r is about 2 times of the classical one (n = 0.079); on the other hand, when operated at a low inlet pre-swirl ratio, n_s is about 2.5 times of the value (n = 0.079) used in a classical Blasius friction model. Notable, when increasing the inlet pre-swirl ratio (α), the CFD obtained n_r remains constant, while n_s decreases with α.

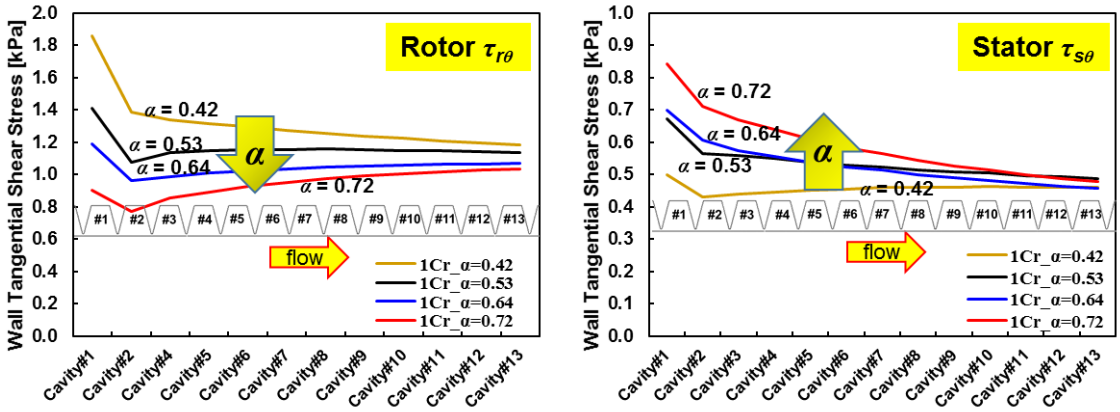

(a) $\tau_{r\theta}$ (b) $\tau_{s\theta}$

Figure 23. Circumferential wall shear stresses $\tau_{r\theta}$ and $\tau_{s\theta}$ vs. cavity number for operation at four inlet pre-swirl ratios α = 0.42-0.72. TOS LS (1C$_r$): P_{in} = 7.3 MPa, P_{out} = 5.1 MPa, rotor speed = 12 krpm.

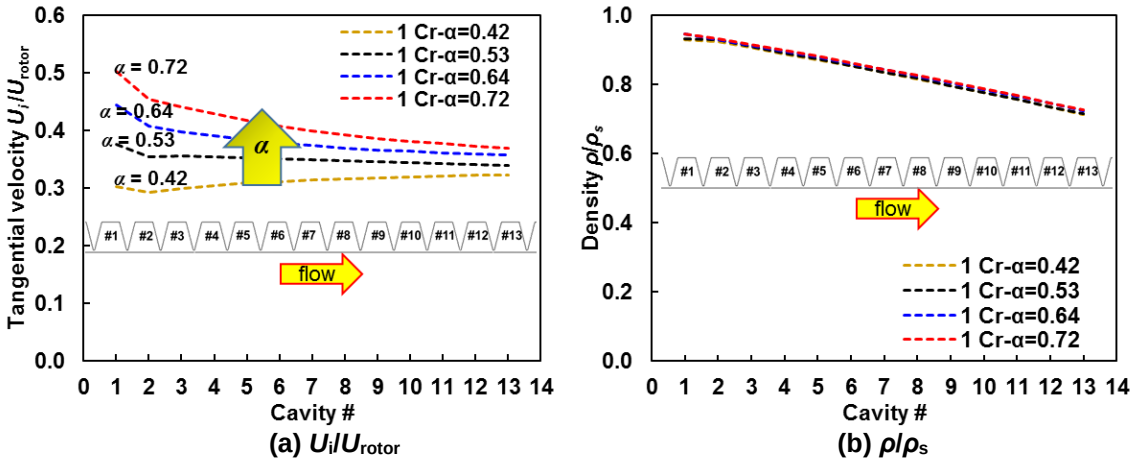

(a) U_i/U_{rotor} (b) ρ/ρ_s

Figure 24. Circumferential velocity U_i/U_{rotor} and density ρ/ρ_s vs. cavity number for operation at four inlet pre-swirl ratios α = 0.42-0.72. TOS LS (1C$_r$): P_{in} = 7.3 MPa, P_{out} = 5.1 MPa, rotor speed = 12 krpm.

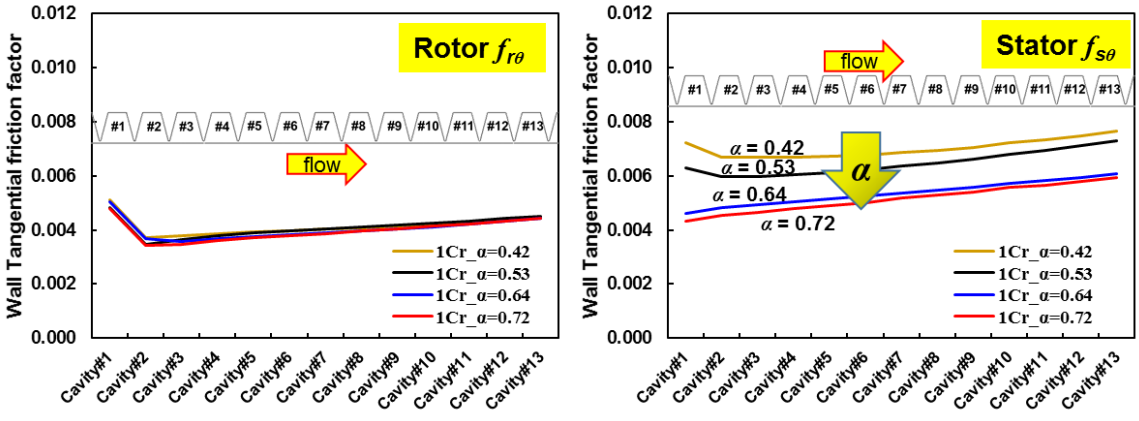

(a) $f_{r\theta}$ (b) $f_{s\theta}$

Figure 25. Friction factor $f_{r\theta}$ and $f_{s\theta}$ vs. cavity number for operation at four inlet pre-swirl ratios α = 0.42-0.72. TOS LS (1C$_r$): P_{in} = 7.3 MPa, P_{out} = 5.1 MPa, rotor speed = 12 krpm.

Table 6. New friction factor coefficients (*n*, *m*) obtained for four inlet pre-swirl ratios.

α	n_r	m_r	n_s	m_s
0.42	0.14	-0.25	0.20	-0.25
0.53	0.14		0.19	
0.64	0.14		0.17	
0.72	0.14		0.16	

6. CLOSURE

This report presents a CFD analysis of a TOS LS to quantify the effect of seal clearance and operating conditions on the wall surface friction factors ($f_{r\theta}$, $f_{s\theta}$). Based on a TOS LS presented by Vannini et al. [52] and tested in 2014, the radial clearance varies from 0.8 C_r (0.24 mm) to 1.2 C_r (0.36 mm), and the rotor speed increases from 5 krpm to 15 krpm ($R\Omega$ = 58 ~173 m/s). The supply pressure ranges from 60 bar to 100 bar, and the pressure ratio PR varies from 0.40 to 0.85. In addition, the inlet pre-swirl velocity ratio $\alpha = U_0/(R\Omega) = 0.42\sim0.72$.

The CFD predictions show the traditional Blasius friction factor model underestimates the friction factors on both rotor and stator surfaces. The rotor surface friction factor $f_{r\theta}$ is independent of (modest) changes (±20%) in clearance (C_r) or the inlet presiwrl ratio (α); whereas an increase in rotor speed (Ω) or pressure ratio (PR) decreases $f_{r\theta}$. On the other hand, an increase in rotor speed (Ω), pressure ratio (PR) and inlet preswirl ratio decreases $f_{s\theta}$, the stator friction factor. Besides, $f_{s\theta}$ increases with an increase in radial clearance (C_r). CFD predictions show that $f_{r\theta}$ and $f_{s\theta}$ are only sensitive to the pressure ratio, but not to the magnitude of the supply pressure or discharge pressure.

The CFD predictions deliver a set of new coefficients (n, m) for the friction factor $f=nRe^m$ and affected by changes in tip clearance and operating conditions. The CFD (n, m)'s are larger than those from the classical formula, n = 0.79, m = -0.25. Hence denoting the classical f model under estimates the rotor and stator wall friction factors. A forthcoming multivariable analysis will later deliver more adequate correlations with (n,m) as functions of the considered parameters.

Later, integration of these relations into a BFM code will will improve its accuracy to predict the evolution of the circumerential flow velocity and the seal rotordynamic force coefficients, the cross-coupled stiffness in particular.

7. NOMENCLATURE

a_r, a_s	Dimensionless length defined in Eqn. (3).
A	Cross-sectional area of the cavity [m^2]
B	Height of the labyrinth seal strip [mm]
C_r	Radial clearance [mm]
D	Rotor diameter [mm]
D_h	Hydraulic diameter, $D_{hi} = 2(C_r + B)L_i/(C_r + B + L_i)$ [mm]
f	Friction factor, $f_{r,s} = n_{r,s}Re^{m_{r,s}}$
h	Local radial clearance [mm]
L	Seal length [mm]
L_i	Pitch length [mm]
L_t	Tooth width [mm]
n_r, m_r, n_s, m_s	Empirical coefficients for *Blasius* friction factor
NT	Number of tooth
P_i	i^{th} cavity pressure [Pa]
P_{in}, P_{out}	Supply/discharge pressure [Pa]
PR	Pressure ratio, $PR = P_{in}/P_{out}$
Re	Reynolds number, $Re_{r,s} = U_{r,s}D_h/\nu$
R_g	Gas constant
R	Rotor radius [mm]
T	Temperature [K]
U	Bulk-flow circumferential velocity in a cavity [m/s]
$U_{r,s}$	Relative bulk-flow velocity, $U_r = \sqrt{W^2 + (U - R\Omega)^2}, U_s = \sqrt{W^2 + U^2}$
U_{rotor}	Rotor surface velocity $U_{rotor} = R\Omega$ [m/s]
U_0	Inlet pre-swirl velocity [m/s]
V_s	Sound speed [m/s]
W	Bulk-flow axial velocity [m/s]
Z_g	Compressibility factor
α	Inlet pre-swirl ratio, $\alpha = U_0/(R\Omega)$
γ	Specific heats ratio
Θ	Circumferential direction
μ_{1i}	Kinetic energy carry-over coefficient
μ_{2i}	Flow discharge coefficient
ν	Kinematic viscosity $\nu = \mu/\rho$ [m^2/s]
ρ	Density [kg/m^3]
ρ_s	Density at supply pressure[kg/m^3]
τ	Shear stress [N]
Ω	Rotor speed [rpm]

Subscripts

i	i^{th} chamber value
r	Rotor surface
s	Stator surface

Abbreviations

BFM	Bulk-flow model
CFD	Computational fluid dynamics
LS	Labyrinth seal
TOS	Tooth on stator labyrinth seal

8. REFERENCES

[1] Ek, M., 1978, "Solution of the Subsynchronous Whirl Problem in the High-Pressure Hydrogen Turbomachinery of the Space Shuttle Main Engine," 14th Joint Propulsion Conference,Las Vegas, July 25-27, pp. 100201-100226.

[2] Childs, D. W., 1993, *Turbomachinery Rotordynamics: Phenomena, Modeling, and Analysis*, Chap.5, "Rotordynamic Models for Annular Gas Seals", John Wiley & Sons.

[3] Kuwamura, Y., Matsumoto, K., Uehara, H., Ooyama, H., Tanaka, Y., and Nishimoto, S., 2013, "Development of New High-Performance Labyrinth Seal Using Aerodynamic Approach," ASME Paper GT2013-94106.

[4] Gao, R., and Kirk, G., 2013, "CFD Study on Stepped and Drum Balance Labyrinth Seal," Tribol T, **56**(4), pp. 663-671.

[5] Benckert, H., and Wachter, J., 1978, "Studies on Vibrations Stimulated by Lateral Forces in Sealing Gaps," AGARD Seal Technology in Gas Turbine Engineering, UK.

[6] Childs, D. W., 1993, *Turbomachinery Rotordynamics: Phenomena, Modeling, and Analysis*, Chap.4, "Rotordynamic Models for Annular Gas Seals", John Wiley & Sons.

[7] Leong, Y., and Brown, R., 1984, "Experimental Investigation of Lateral Forces Induced by Flow through Model Labyrinth Glands," Proceedings of a Workshop on Rotordynamic Instability Problems in High-Performance Turbomachinery,Texas A&M University, College Station, TX, pp. 187-210.

[8] Childs, D. W., and Scharrer, J. K., 1986, "Experimental Rotordynamic Coefficient Results for Teeth-on-Rotor and Teeth-on-Stator Labyrinth Gas Seals," ASME J Eng Gas Turb Power, **108**(4), pp. 599-604.

[9] Thieleke, G., and Stetter, H., 1990, "Experimental Investigations of Exciting Forces Caused by Flow in Labyrinth Seals," Proceeding of a Workshop on Rotordynamic Instability Problems in High-Performance Turbomachinery,Texas A&M University, College Station, TX, pp. 109-134.

[10] Childs, D. W., Elrod, D. A., and Hale, K., 1988, "Rotordynamic Coefficient and Leakage Test Results for Interlock and Tooth-on-Stator Labyrinth Seals," ASME Paper 88-GT-87.

[11] Paolillo, R., Moore, S., Cloud, D., and Glahn, J. A., 2007, "Impact of Rotational Speed on the Discharge Characteristic of Stepped Labyrinth Seals," Turbo Expo. 2007, ASME Paper GT2007-28248.

[12] Li, Z., Li, J., Yan, X., and Feng, Z., 2011, "Effects of Pressure Ratio and Rotational Speed on Leakage Flow and Cavity Pressure in the Staggered Labyrinth Seal," ASME J Eng Gas Turb Power, **133**(11), pp. 11450301-11450306.

[13] Gamal, A. J., and Vance, J. M., 2008, "Labyrinth Seal Leakage Tests: Tooth Profile, Tooth Thickness, and Eccentricity Effects," ASME J Eng Gas Turb Power, **130**(1), pp. 01251001-01251011.

[14] Hodkinson, B., 1939, "Estimation of the Leakage through a Labyrinth Gland," Proceedings of the Institution of Mechanical Engineers, **141**(1), pp. 283-288.
[15] Zhang, L., Zhu, H., Liu, C., and Tong, F., 2016, "Experimental and Numerical Investigation on Leakage Characteristic of Stepped Labyrinth Seal," ASME Paper GT2016-56743.
[16] Picardo, A., and Childs, D. W., 2005, "Rotordynamic Coefficients for a Tooth-on-Stator Labyrinth Seal at 70 Bar Supply Pressures: Measurements versus Theory and Comparisons to a Hole-Pattern Stator Seal," ASME J Eng Gas Turb Power, **127**(4), pp. 843-855.
[17] Wagner, N. G., Steff, K., Gausmann, R., and Schmidt, M., 2009, "Investigations on the Dynamic Coefficients of Impeller Eye Labyrinth Seals," Proc. of the 38th Turbomachinery Symposium, Houston, TX, September 14-17.
[18] Ertas, B. H., Delgado, A., and Vannini, G., 2012, "Rotordynamic Force Coefficients for Three Types of Annular Gas Seals with Inlet Preswirl and High Differential Pressure Ratio," ASME J Eng Gas Turb Power, **134**(4), pp. 042503-042512.
[19] Vannini, G., Cioncolini, S., Del Vescovo, G., & Rovini, M. , 2014, "Labyrinth Seal and Pocket Damper Seal High Pressure Rotordynamic Test Data," ASME J Eng Gas Turb Power, **136**(2), pp. 022501-022509.
[20] Murphy, B., and Vance, J., 1980, "Labyrinth Seal Effects on Rotor Whirl Instability," Proceedings of the 2nd International Conference on Vibrations in Rotating Machinery,Cambridge, England, September 1-4.
[21] Kostynk, A., 1972, "Theoretical Analysis of the Aerodynamic Forces in the Labyrinth Glands of Turbomachines," Therm Eng, **19**(11), pp. 29-33.
[22] Iwatsubo, T., 1980, "Evaluation of Instability Forces of Labyrinth Seals in Turbines or Compressors," Proceedings of a Workshop on Rotordynamic Instability Problems in High-Performance Turbomachinery,Texas A&M University, College Station, TX, pp. 139-167.
[23] Iwatsubo, T., Motooka, N., and Kawai, R., 1982, "Flow Induced Force of Labyrinth Seal," Proceedings of a Workshop on Rotordynamic Instability Problems in High-Performance Turbomachinery,Texas A&M University, College Station, TX, pp. 205-222.
[24] Childs, D. W., and Scharrer, J. K., 1986, "An Iwatsubo-Based Solution for Labyrinth Seals: Comparison to Experimental Results," ASME J Eng Gas Turb Power, **108**(2), pp. 325-331.
[25] Martin, H., 1908, "Labyrinth Packings," Engineering, **85**(10), pp. 35-38.
[26] Egli, A., 1935, "The Leakage of Steam through Labyrinth Seals," Trans. Asme, **57**(3), pp. 115-122.
[27] Neumann, K., 1964, "Zur Frage der Verwendung von Durchblickdichtungen im Dampfturbinenbau," Maschinenbautechnik, **13**(4), pp. 188-195.
[28] Hirs, G. G., 1973, "A Bulk-Flow Theory for Turbulence in Lubricant Films," ASME J Lubric Tech, **95**(2), pp. 137-145.
[29] Yamada, Y., 1962, "Resistance of a Flow through an Annulus with an Inner Rotating Cylinder," Bulletin of JSME, **5**(18), pp. 302-310.
[30] Al-Qutub, A. M., Elrod, D., and Coleman, H. W., 2000, "A New Friction Factor Model and Entrance Loss Coefficient for Honeycomb Annular Gas Seals," ASME J. Tribol, **122**(3), pp. 622-627.
[31] Villasmil Urdaneta, L., 2002, "Understanding The Friction Factor Behavior in Liquid Annular Seals with Deliberately Roughened Surfaces, A CFD Approach," M.S Thesis, Texas A&M University, College Station, USA.

[32] Villasmil Urdaneta, L., 2006, "Parameters Defining Flow Resistance and The Friction Factor Behavior in Liquid Annular Seals With Deliberately Roughened Surfaces," Ph.D Thesis, Texas A&M University, College Station, USA.
[33] D'Souza, R., and Childs, D. W., 2002, "A Comparison of Rotordynamic-Coefficient Predictions for Annular Honeycomb Gas Seals Using Three Different Friction-Factor Models," ASME J. Tribol, **124**(3), pp. 524-529.
[34] Moore, J. J., 2003, "Three-Dimensional CFD Rotordynamic Analysis of Gas Labyrinth Seals," ASME J Vib Acoust, **125**(4), pp. 427-433.
[35] Kwanka, K., 2001, Der Einfluss von Labyrinthdichtungen auf die Dynamik von Turbomaschinen, Fortschritt-Bericht VDI-Verlag.
[36] Wagner, N. G., 1999, "Reliable Rotor Dynamic Design of High-Pressure Compressors Based on Test Rig Data," ASME Paper 99-GT-150.
[37] Schettel, J., Deckner, M., Kwanka, K., Lüneburg, B., and Nordmann, R., 2005, "Rotordynamic Coefficients of Labseals for Turbines: Comparing CFD Results With Experimental Data on a Comb-Grooved Labyrinth," Turbo Expo. 2005, ASME Paper GT2005-68732.
[38] Kim, T. S., and Cha, K. S., 2009, "Comparative Analysis of The Influence of Labyrinth Seal Configuration on Leakage Behavior," J Mech Sci Technol, **23**(10), pp. 2830-2838.
[39] Kim, T. S., and Kang, S. Y., 2010, "Investigation of Leakage Characteristics of Straight and Stepped Labyrinth Seals," International Journal of Fluid Machinery and Systems, **3**(3), pp. 253-259.
[40] Kang, Y., Kim, T. S., Kang, S. Y., and Moon, H. K., 2010, "Aerodynamic Performance of Stepped Labyrinth Seals for Gas Turbine Applications," Turbo Expo. 2010, ASME Paper GT2010-23256.
[41] Pugachev, A. O., and Deckner, M., 2010, "Analysis of the Experimental and CFD-Based Theoretical Methods for Studying Rotordynamic Characteristics of Labyrinth Gas Seals," Turbo Expo. 2010, ASME Paper GT2010-22058.
[42] Pugachev, A. O., Kleinhans, U., and Gaszner, M., 2012, "Prediction of Rotordynamic Coefficients for Short Labyrinth Gas Seals Using Computational Fluid Dynamics," ASME J Eng Gas Turb Power, **134**(6), pp. 06250101-06250110.
[43] Pugachev, A. O., and Degen, H., 2012, "CFD-Predicted Rotordynamic Coefficients for a 20-Teeth-on-Stator Labyrinth Seal at High Supply Pressure Conditions," Turbo Expo. 2012, ASME Paper GT2012-68381.
[44] Dai, Y., Tyacke, J., and Tucker, P., 2016, "Effect of Labyrinth Seal Configurations on Leakage Performance using LES," 54th AIAA Aerospace Sciences Meeting, San Diego, California, USA.
[45] Rai, A. C., Prabhudharwadkar, D., Murthy, S., Giametta, A., and Johns, D., 2016, "Effect of Air-Curtains on Labyrinth Seal Performance," Turbo Expo. 2016, ASME Paper GT2016-57188.
[46] Migliorini, P. J., Untaroiu, A., Wood, H. G., and Allaire, P. E., 2012, "A Computational Fluid Dynamics/Bulk-Flow Hybrid Method for Determining Rotordynamic Coefficients of Annular Gas Seals," ASME J Tribol, **134**(2), pp. 0222021-0222029.
[47] Migliorini, P. J., Untaroiu, A., Witt, W. C., Morgan, N. R., and Wood, H. G., 2014, "Hybrid Analysis of Gas Annular Seals with Energy Equation," ASME J Tribol, **136**(3), pp. 0317041-0317049.

[48] Childs, D. W., and Wade, J., 2004, "Rotordynamic Coefficient and Leakage Characteristics for Hole-Pattern-Stator Annular Gas Seals-Measurements versus Predictions," ASME J Tribol, **126**(2), pp. 326-333.
[49] San Andrés, L., Wu, T., Maeda, H., and Ono, T., 2018, "A Computational Fluid Dynamics Modified Bulk-Flow Analysis for Circumferentially Shallow Grooved Liquid Seals," ASME J Eng Gas Turb Power, **140**, pp. 0125041-0125049.
[50] Nordmann, R., Dietzen, F. J., Janson, W., Frei, A., Florjancic, S., 1986, "Rotordynamic Coefficients and Leakage Flow of Parallel Grooved Seals and Smooth Seals."
[51] San Andrés, L., 1991, "Analysis of Variable Fluid Properties, Turbulent Annular Seals," ASME J Tribol, **113**(4), pp. 694-702.
[52] Vannini, G., Cioncolini, S., Del Vescovo, G., and Rovini, M., 2014, "Labyrinth Seal and Pocket Damper Seal High Pressure Rotordynamic Test Data," ASME J Eng Gas Turb Power, **136**(2), pp. 022501-022509.